Version of Record: https://www.sciencedirect.com/science/article/pii/S0169809522002903
Manuscript_51b19bc7ab62f615d6e51ab4bb707910

Impact of Adaptively Thinned GOES-16 All-sky Radiances in an Ensemble Kalman Filter based WoFS

Swapan Mallick[1,2] and Thomas A. Jones[1,2,3]

1. Cooperative Institute for Severe and High Impact Weather Research and Operations (CIWRO), The University of Oklahoma, Norman, OK
2. NOAA/OAR National Severe Storms Laboratory, Norman, OK
3. University of Oklahoma, Norman, OK

Corresponding Author Address:

Dr. Swapan Mallick
Cooperative Institute for Severe and High Impact Weather Research and Operations (CIWRO) and
NOAA/OAR National Severe Storms Laboratory
120 David L. Boren Blvd.
Norman, OK 73072
E-mail: smallick04@gmail.com

Abstract

The ability to forecast severe weather events can be improved by assimilating GOES-16 satellite observations into high-resolution convective scale numerical weather prediction models. In this study, multiple sensitivity experiments were performed for four severe weather events that occurred on 7 May, 21 June 2020; and 7, 23 May 2021. Our goal is to assess how the application of data thinning techniques on the GOES-16 all-sky radiance data assimilated by the National Severe Storms Laboratory's ensemble-based Warn-on-Forecast System (WoFS) affect subsequent weather forecasts. A total of three experimental configurations are considered for this analysis: (1) ABI-TH, an adaptive-based data thinning method used in the cloudy region; (2) ABI-ALL, in which all available all-sky radiances were assimilated; and (3) CNTL, a control experiment that used cloud water path (CWP) data but assimilated no radiance data. All three experiments assimilated conventional, radar reflectivity, and radial velocity observations. For each experiment, multiple sensitivity tests are performed to assess the effect of thinning the GOES-16 all-sky radiance data assimilated by the WoFS using an object-based verification method in which model-simulated composite reflectivity and 2-5 km Updraft Helicity (UH) fields were compared to Multi-Radar Multi-Sensor (MRMS) reflectivity and rotation objects. In addition, synthetic satellite images from the WoFS output are generated and compared with the synthetic visible and infrared images from GOES-16. Results show that the ABI-TH approach produced better forecasts relative to ABI-ALL for high-impact weather events. The results from ABI-TH are also similar to results from CWP assimilation (CNTL).

Key words: GOES-16, All-sky radiance, Ensemble Data Assimilation, Short-range prediction, GSI-EnKF, Superobbing satellite data, CRTM, RTTOV.

1. Introduction

Modern data assimilation techniques are critically important for improving the quality of numerical weather prediction and taking maximum advantage of the wide variety of available observations, including high-resolution satellite data. High-resolution satellite data are especially important for initializing cloud properties in the assimilation system (Gregow et al., 2020). At the same time, it is important to understand the factors that influence how satellite observations can affect forecasts. For example, the impact of satellite observations on weather forecasts may change over domains, time (i.e., how and where the data are used), and the evolution of the assimilation system (McNally, 2014). Key steps in fine-tuning the data assimilation system include quality control, observation error, and data thinning. Poorly specified background or observation errors may influence the impact an observation has on the forecast. Careful consideration of data assimilation evolution can prevent researchers from making incorrect decisions about the usefulness of available satellite data (Bormann et al., 2019).

Dense satellite data can severely violate the assumption that satellite observation errors are independent (Ochotta et al. 2005), which is a basic requirement of satellite data assimilation systems (Reale et al. 2018). In a data assimilation system, computational considerations and the use of high-quality data are important. One consideration when using dense observations is “superobbing,” which is a method used to thin data before data assimilation. Superobbing is required when assimilating dense satellite data (Berger and Forsythe, 2004; Janjić et al., 2018). Many studies have discussed the importance of satellite observation error and data thinning methods. If observation errors are uncorrelated, using more observations should reduce the analysis error (Chang, 2014). However, observation errors are not always uncorrelated, which is why thinning should be performed to reduce analysis error. Increasing the amount of satellite data beyond a certain threshold adds little new information to the data assimilation system if the observation errors are correlated (Liu and Rabier, 2002). One of the important roles of superobbing is to avoid the difficulty of explicitly treating correlated observation errors in a data assimilation system (Kazumori, 2014). Superobbing is used to reduce random errors in the observations and to reduce the correlation between observation errors (Lu and Xu, 2009).

Multiple experiments have tested the effect of superobbing satellite wind using the United Kingdom Met-Office (UKMO) global model (Berger and Forsythe, 2004). The results show that superobbing has a positive effect on forecasts in the northern hemisphere but a slightly negative effect in the southern hemisphere. The overall impact was neutral when only a percentage of all available satellite wind data was used. To minimize the potential negative impact superobbing can have on the analysis, superobbing algorithms are designed to retain as much independent information in the observations as possible while reducing correlated error. A variety of methods have also been used for superobbing radar data (Majcen et al., 2008; Aksoy et al., 2009; Salonen et al., 2009; Dowell et al., 2011; Kerr et al., 2021). For example, an adaptive superobbing technique has been used to remove radar radial velocities that minimally impact analyses and forecasts and only add noise to the model state (Kerr and Wang, 2020). One of the important research topics in satellite data assimilation systems is designing a smart thinning procedure that contains the most informative spot in each thinning box (Thepaut 2003).

In this study, an attempt is made to assimilate all-sky radiance information from high-resolution GOES-16 satellite data. The uncertainty in modeling hydrometeors and the inaccuracy of the model simulating cloudy radiances made it difficult to assimilate radiances in the presence of clouds (Auligné and Wang, 2012; Liu et al., 2012; Xu et al., 2013; Tavolato and Isaksen, 2015). In addition, few studies have assimilated all-sky radiance data (including cloud-affected radiance), though clear-sky radiance data has been widely assimilated for many years. Many studies have discussed the importance of clear-sky radiance assimilation for improving the accuracy of weather analyses and forecasts (McNally, 2009; Pangaud et al., 2009; Mallick et al., 2016; Mallick et al., 2017; Sharma et al., 2016; Srinivas et al., 2016; Shi et al., 2018; Jones et al., 2018a). For example, Yang et al. (2017) showed that assimilating clear-sky radiance data from the GOES imager using a rapid refresh assimilation system with a hybrid-3DEnVar scheme could improve convection-permitting forecasts. Nevertheless, including information about cloudy areas by using all-sky radiance in the assimilation system has the potential to further improve forecast quality.

Assimilation of all-sky radiance increases the number of observations available in cloudy areas and provides more information on temperature and moisture in those areas (Geer et al., 2018, 2019; Li et al., 2021). All-sky assimilation approaches, even if hydrometeor information is not assimilated, also avoid the biases of the clear-sky approach that are caused by undetected clouds or asymmetric sampling (Zhu et al., 2016; Geer et al., 2017). Geer and Bauer (2011) demonstrated that there is more uncertainty in cloudy radiance assimilation than in clear-sky radiance assimilation, and that errors can vary with atmospheric conditions. Otkin (2012) showed that the assimilation of cloudy radiances measured using thermal infrared bands, alongside strict quality control measures, can improve predictions of convective-scale severe storms. Minamide and Zhang (2017) demonstrated the effects of an adaptive observation error inflation method for ensemble-based all-sky radiance assimilation. Their data thinning method was designed to limit incorrect analysis increments when there are large representativeness errors in cloudy radiance data. Zhang et al. (2018) assimilated all-sky radiances measured from GOES-16 water vapor bands. Their method improved forecasts of cloud properties, severe convective initiation, and near-storm environments compared to experiments that only assimilated radar data.

Our goal was to assess the impact of all-sky radiance assimilation on the National Severe Storms Laboratory (NSSL) Warn on Forecast (WoFS) system. This study investigated the effect of assimilating GOES-16 radiances from water vapor channels into the WoFS system. Four high-impact severe weather events that occurred on 7 May 2020, 21 June 2020, and 7, 23 May 2021 are considered in this study. Observation increment statistics are computed against the model background for quality assessment and are used to measure their impact on the mesoscale environment within the model. Results from superob analyses of the GOES-16 data are discussed and verified using different object-based statistical methods. Section 2 of this paper describes the satellite-retrieved GOES-16 radiance products, the data assimilation and forecast system (WoFS), and the overall experimental design. Section 3 details how radiance superob analyses affected reflectivity and updraft helicity (UH) forecasts and synthetic satellite images. Overall discussion and conclusions are presented in Section 4.

2. GOES-16 imager

Across the continental USA, satellite data collected from the Advanced Baseline Imagers (ABI) installed on the GOES-R series of geostationary satellites have been used extensively by operational weather forecasting centers. The GOES-R ABI scans 16 different spectral bands over the Western hemisphere at various time intervals. The special resolution of the images is 0.5, 1, and 2-km in the visible, near infrared, and infrared wavelengths. The ABI has three scanning and imaging modes: the full disk mode takes images every 15 mins, the Continental US mode (CONUS, 5000 km X 3000 km) takes images every 5 minutes, and the mesoscale mode (1000 km X 1000 km) takes images every 1 minute. Further details on the GOES-16 ABI and its channel characteristics can be found in Schmit et al. (2005, 2017).

The GOES-16 radiance observations from the real-time L1B product are used as the starting point. For all-sky radiance assimilation, the three ABI bands used that are sensitive to atmospheric water vapor. These bands have wavelengths from 5.5–7.5 µm. The thermal infrared channels 8 (6.2 µm), 9 (6.9 µm) and 10 (7.3 µm) are sensitive to upper, middle, and low-level atmospheric water vapor content. The 6.2 and 6.9 µm bands are mainly used for estimating upper and mid-level moisture, tracking upper-tropospheric and mid-level winds, identifying jet streams and mid-latitude storm motion, monitoring severe weather potential, searching for signatures of potential turbulence, and validating model initialization and forecast. Surface features are not apparent in these two bands, and the brightness temperature decreases (i.e., shows cooling) as energy is absorbed by water vapor. The 7.3 µm band is used to explore further down into the mid-troposphere in cloud-free regions (~500-750 hPa). This band is also used to track lower tropospheric winds, monitor severe weather potential, identify jet streams, estimate lower-level moisture, track lake-effect snow bands, and highlight volcanic plumes.

Before the water vapor bands are assimilated into the WoFS, multiple data preprocessing steps were performed with the available radiance data including quality control, data thinning, and parallax correction. The radiance data were first converted to brightness temperature by inversion using Planck's equation (Kidder and Vonder Haar, 1995). For cloud information, we combined cloud top height information from the L2 ACHAC product with the L1B data and fit them to the 5 km grid space. To reduce the displacement error caused by cloudy pixels, a parallax correction for cloudy radiances (Lábó and Putsay, 2007; Wang and Huang, 2014) were applied. In the clear-sky regions, the 6.2 µm and 7.3 µm channels at a 15 km grid spacing are assimilated. The 6.9 µm channel is not assimilated as 6.9 µm channel have high correlation with the 6.2 µm and 7.3 µm channels (Honda et al. 2018). High correlation between channels indicates little independent information to the assimilation system. In addition to that only the 7.3 µm channel with full 5 km resolution are assimilated for cloudy regions. This is because both 6.2 µm and 7.3 µm channels are high correlation and assimilating high correlated both the channels resulting in a cloudy bias in the model (Zhang et al. 2018). Further details are provided by Jones et al. (2020).

3. Model configuration and assimilation method

a. Ensemble Configuration:

Multiple data assimilation techniques have been developed for operational frameworks and include variational solvers (3DVAR and 4DVAR; Courtier and Talagrand, 1987; Klinker et al., 2000; Barker, 2004; Fischer et al., 2005, Hu, et al., 2006; Rawlines et al., 2007; Tanguay et al., 2007; Bonavita et al., 2012; Sun and Wang, 2013; George et al., 2016), ensemble Kalman filters (EnKF; Snyder and Zhang, 2003; Anderson and Collins, 2007; Dowell et al., 2011; Bick et al., 2016), and hybrid methods (3D/4D-Var + EnKF); Clayton et at., 2013; Penny, 2014; Kleist and Ide, 2015; Bonavita et al., 2016; Tong et al., 2018; Lei et al., 2021; Lu and Wang, 2021). All three methods use a combination of observations and model background fields to calculate more accurate and dynamically consistent initial conditions. One of the advantages of ensemble data assimilation systems are that these systems can estimate the evolution of the background error covariance matrix from one assimilation cycle to the next (Bonavita et al., 2012, Pan et al., 2014).

The WoFS system (Wheatley et al., 2015; Jones et al., 2016; Skinner et al., 2018; Jones et al., 2018; Jones et al., 2019; Mallick and Jones, 2020; Jones et al., 2020; Wang et al., 2021) generates short-term 0-6 h forecasts of high-impact weather events including severe thunderstorms, tornadoes, heavy rainfall, large hail, flash floods, and landfalling tropical cyclones. The location of the 3-km WoFS domain is the most likely region for the development of severe convection and is determined based on the Storm Prediction Center's one-day convective outlook. The WoFS is a 36-member ensemble-based data assimilation and forecasting system; it uses the Grid-point Statistical Interpolation (GSI) package, which includes an EnKF for its data assimilation system (Whitaker and Hamill, 2002; DTC 2017). Every 15 minutes, the WoFS produces ensemble analyses using the EnKF technique. The Advanced Research version of the Weather Research and Forecasting Model (WRF-ARW version 3.9; Skamarock et al., 2008) is used during system cycling and for weather forecasts. The 18-member forecasts are issued every half-hour beginning at 1900 UTC and ending at 0000 UTC.

All 36 ensemble members use the NSSL two-moment cloud microphysics scheme (Mansell et al., 2010). The High-Resolution Rapid Refresh ensemble (HRRRE) provides the boundary and initial conditions used to initialize the WoFS analyses. A covariance localization is used by the GSI-EnKF system for all observations assimilated into the model, including conventional, radar, and satellite data (Table 1). For CWP, covariance localizations were set to 36 km in the horizontal direction and 0.9 scale height in the vertical direction. For all-sky and clear-sky radiance, horizontal and vertical localizations were set to 36 km and 4.0, respectively. This localization parameters are similar to those used by Jones et al. (2020) and Mallick and Jones (2020). Table 1 provides a complete list of all observations, observation errors, and covariance localizations used in this study. The conventional data set used by the model includes surface temperature, pressure, humidity, and wind measurements from the available Oklahoma Mesonet and Automated Surface Observing System (ASOS) sites. Radar radial velocity from level 2 WSR-88D data was also assimilated into the WoFS. During the observation preprocess, these data were objectively analyzed to 5 km resolution using the Cressman scheme. WSR-88D reflectivity was also contained within the 1 km MRMS products and objectively analyzed to 5 km resolution (Smith et al., 2016). CWP observations from the GOES-16 are obtained using the Satellite Cloud and Radiation Property Retrieval System (SatCORPS) developed by the NASA Langley research center (Minnis et al., 2011, Jones et al., 2016). The GOES-R Clouds Algorithm Working Group uses the visible infrared solar-infrared split-window technique (VISST) to retrieve daytime cloud properties and the Shortwave-Infrared Infrared Split-window Technique (SIST) to retrieve nighttime cloud properties. Daytime CWP data are retrieved from the GOES-R channels (2, 7), which have wavelengths of 0.64 and 2.25 µm, respectively, and nighttime CWP data are retrieved from the GOES-R channels (7, 14, 15), which have wavelengths of 3.9, 11.2, and 12.3 µm, respectively. The CWP data are then used to determine cloud optical and microphysical properties (COMP). In this study, only daytime CWP data collected from channels in the visible and a short-wave infrared band are used. At nighttime without the visible channel data in the retrieval algorithm, biases and error characteristics differ significantly from the daytime retrievals. In this study, all the forecasts are initialized at daytime data assimilation cycle (upto 0000 UTC) and the nighttime CWP data are available from 0100 UTC onward. The details of the CWP forward operator are available in Jones and Stensrud (2015) and Jones et al. (2016). The CWP observation errors are based on the uncertainty characteristics of the retrieval algorithm and is defined as a function of both liquid water path (LWP) and Ice water path (IWP) values. The lowest observation errors defined for clear-sky retrievals and the highest defined for high CWP retrievals. For CWP = 0, the observation error is 0.025 kg/m2 and for CWP > 2.5 kg/m2, the observation error is 0.2 kg/m2 Table 1). Further details of CWP observation error are provided by Jones et al. (2015).

b. Overviews of the selected cases

To assess the potential effects of applying adaptive data assimilation method for GOES-16 all-sky radiances in the WoFS, total four high-impact weather events were considered: two from 2020, and two from 2021. Table 2 and Fig. 1 show the Storm Prediction Center (SPC) reports of tornadoes, severe hail (diameter > 1.0 in.), and high winds within the study area of each event. Fig. 1 also provide the MRMS composite reflectivity and the GOES-16 low-level water vapor (7.3 μm) brightness temperature (K) at 0000 UTC analysis time within the domain of each event. On 7 May 2020, an isolated supercell thunderstorm produced a long swath of large hail across northern Texas. Throughout the evening and into the night, multiple thunderstorms occurred over the northwest part of Oklahoma, and there were multiple hail reports over the adjacent parts of Texas and near southwest Oklahoma. On 21 June 2020, a severe storm system affected portions of south-central and central Kansas. Numerous severe storms occurred from early evening into the night, mainly across portions of southern Kansas, Nebraska and Oklahoma. Damaging winds and isolated large hail occurred across the study domain, though there were no reports of any tornadoes. On 7 May 2021, surface heating and deep mixing promoted the development of late-afternoon severe thunderstorms over New Mexico. The storms persisted longer across the Texas and Oklahoma Panhandle and toward northwest Oklahoma, where a low-level jet maintained stronger low-level warm advection. The stronger updrafts and the midlevel lapse rates supported multiple hail events over Texas and Oklahoma. By midafternoon on 23 May 2021, scattered thunderstorm had developed over several areas in South Dakota, Nebraska, and Colorado. The primary severe weather threats were hail and wind, though isolated supercells in Colorado and Wyoming produced several tornadoes. The most likely corridor for tornadoes, large hail, and severe wind was across northeast Colorado and southwestern portions of Nebraska.

c. GOES-16 all-sky radiance assimilation techniques

This section investigates how assimilating all-sky radiances from the GOES-16 water vapor channels (6.2 μm and 7.3 μm) affects the WoFS system. This investigation tested three different experimental configurations. The first approach, ABI-TH, used an adaptive-based data thinning method for cloudy observations. In the ABI-TH approach, both channels are assimilated in the clear-sky regions as before, but only the 7.3 μm channel radiances are assimilated in cloudy regions if the difference between the observed (O) and simulated (B) brightness temperatures from the Community Radiative Transfer Model (CRTM) is greater than 10 Kelvin (K) (i.e., |O-B| > 10 K). The CRTM is a widely used fast radiative transfer model developed by the Joint Center for Satellite Data Assimilation (Weng, 2007; Han et al., 2007). For the experiment, referred to as ABI-ALL, both 6.2 μm and 7.3 μm channels are assimilated in the clear-sky regions, and in cloudy regions, all available radiances from the 7.3 μm channel are assimilated. The third experiment, CNTL, served as a control; this experiment used a configuration that did not assimilate any radiance data but included CWP data (similar to real-time version). Several sensitivity experiments have been performed with |O-B| > 1K, 2K, 5K, 10K and 15K for ABI-TH. It has been observed that the number of assimilated observations are similar to ABI-ALL experiments, and the forecast skill are nearer to ABI-ALL experiments with |O-B| > 1K or 2K or 5K. Further, with |O-B| > 15K only 10% of total cloudy radiance assimilated. This means most of the data having cloud information are rejected and are not used in the assimilation system with |O-B| > 15K. And hence, the optimal configuration with |O-B| > 10 K is used in the thinning approach for cloudy observations.

For radiance assimilation in these experiments, the CRTM is used as a forward operator to generate simulated brightness temperature. It is noted that radiative transfer models themselves have biases and must be taken care of in data assimilation (Zou et al., 2016). We used the level of the maximum Jacobian of the CRTM model-simulated brightness temperature at each data point to determine the vertical level of the observation. The model-simulated brightness temperature was calculated from the background of each ensemble member during each assimilation cycle. The spatial distribution of assimilated 6.2 μm and 7.3 μm bands in the ABI-ALL and ABI-TH data at 2200 UTC, indicating a good representation of clear and cloudy skies within the study domain of each experiment (Fig. 2). The magnitude of the difference in brightness temperature (i.e., O-B) was very large over the cloudy area in the 7.3 μm band, but in clear-sky areas, the (O-B) values were within -2 to 2 K. Observations over in cloudy areas in the ABI-TH approach were retained only when biases (O-B) were more than 10K, but the number of observations in clear-sky areas remains the same for both the ABI-ALL and ABI-TH approaches (Fig. 2).

e. Verification methods

1. *Synthetic satellite data*

The successful assimilation of all-sky radiance into the WoFS system is confirmed by generating multiple synthetic images of simulated GOES-16 channels. This synthetic data was derived using the Radiative Transfer for TOVS (RTTOV-12.3) model applied to WoFS forecasts. The RTTOV model was developed by Saunders et al. (1999) and is maintained by the ECMWF (Matricardi et al., 2004; Saunders at al., 2018). In this study, synthetic satellite data are generated with 3 km resolution using RTTOV-12.3 based on vertical profiles of atmospheric temperatures, water vapor and composition, surface temperatures, and surface wind speed, as well as solar and sensor geometry parameters. For cloudy regions, vertical profiles of hydrometeor data are also used.

2. *Performance diagram*

Performance diagrams (PD) display multiple dichotomous (YES/NO) measures of forecast quality in a single figure (Roebber, 2009). To generate PDs for this study, we combined the critical success index (CSI; Jolliffe and Stephenson, 2003), probability of detection (POD), success ratio (SR), false alarm ratio (FAR), and the frequency of bias (BIAS). The CSI, POD, BIAS, SR and FAR are defined as:

$$\text{CSI} = \frac{A}{A+B+C} \tag{2.1}$$

$$\text{POD} = \frac{A}{A+C} \tag{2.2}$$

$$\text{BIAS} = \frac{A+B}{A+C} \tag{2.3}$$

$$\text{SR} = 1\text{- FAR} = \left(1 - \frac{B}{A+C}\right) \tag{2.4}$$

where A is the number of correct forecasts of a given event, B is the number of forecasted events that were not observed, and C is the number of observed events that were not forecasted (John et al., 2018). CSI, POD and SR approach unity for high-quality forecasts, and a perfect forecast lies in the upper right of the performance diagram.

In this study, the overall model performance is assessed using an object verification method (Skinner et al., 2016, 2018). To quantify the performance of the model-simulated ensemble mean composite reflectively and the 2-5 km updraft helicity forecasts, we computed and aggregated PDs over 3-hr forecasts from 1900 UTC to 0000 UTC at half-hour intervals. All five metrics described above were calculated for a neighborhood radius of 12 km using all the ensemble members of each experiment.

4. Results

a. Observation statistics

For ABI-ALL and ABI-TH, the observation-space diagnostics including the number of assimilated observations and the observation increment (innovation, *O-B*) were calculated (Table 3, Fig. 3). The percentage of assimilated observations in the ABI-TH method were 45%, 52%, 31% and 60% less than in the ABI-ALL model for the 7 May 2020, 21 June 2020, 7 May 2021, and 23 May 2021 weather events, respectively. On average, less than 50% of observations were assimilated with the ABI-TH method compared to the ABI-ALL approach across all four weather events. Fig. 3 shows the number of observations assimilated during each cycle from 1500 UTC to 0300 UTC the following day. Note that the assimilation period on 21 June 2020 started at 1800 UTC, but after 1815 UTC, no observations were available for assimilation until 2000 UTC. On 7 May 2021, large variation in the number of assimilated observations over few assimilation cycles due to the available data has been observed. It is also noted that the number of assimilated observations maintains a similar curve for both the ABI-ALL and ABI-TH methods, although the actual values vary between each assimilation cycle and across methods (Fig. 3).

With respect to observation increment statistics, the prior bias for the ABI-ALL experiment and for all weather events were within the range of -3.2 to 0 K and decreased by approximately 25% after assimilation (post-assimilation bias, *O-A*). This negative value indicates that the model background always overestimates and has systematic biases (Table 4). A similar but stronger negative bias in the ABI-TH experiment (Fig. 3b, d) has been observed. This is because the ABI-TH approach only assimilated observations over cloudy areas if |O-B| > 10K. The spatial distribution of innovation values (*O-B*, *O-A*) over the study domain clearly delineates the all-sky observations that were assimilated in the ABI-ALL and ABI-TH experiments (Fig. 4-7).

For the 8 May 2020 weather event at 0000 UTC, a large systematic bias over the cloudy area at the storm location over the Texas/Oklahoma border was observed. A large number of positive biases within a few kilometers of storm center were found, but negative biases in the surrounding locations in both the ABI-ALL and ABI-TH experiments also existed (Fig. 4). The mean prior biases of ABI-ALL and ABI-TH (-1.59 and -1.72 K, respectively) were similar to each other (Table 4). The ABI-TH approach also used only 55% of the total observations relative to ABI-ALL (Table 3). When just 47% of observations were assimilated, ABI-TH had a large mean prior mean bias of -5.7 K, which decreased to -3.14 K after further assimilation for the 21 June 2020 event (Table 4, Fig. 5). For both the ABI-ALL and ABI-TH experiments, prior biases were randomly distributed across the study domain before assimilation, but we observed a large positive (*O-A*) values reduces over the cloudy area.

On 7 May 2021 at 1900 UTC, only a few cloudy areas were observed over Texas-New Mexico border and southern parts of Colorado (Fig. 6). The total prior biases, and therefore the posterior biases, were lower for this weather event for both ABI-ALL and ABI-TH (Table 4). The ABI-TH approach assimilated 68% of the total observations for this event, meaning that only 32% of observation were discarded during the data thinning process. Across all weather events, this was the highest percentage of assimilated observations relative to ABI-ALL (Table 3). Several systematic prior biases over the convection area have been observed, but the assimilation process only corrected the most positive biases for the 23 May 2021 weather event (Fig. 7). In addition, only 39% of observations were used in the ABI-TH experiment for this weather event (Table 3). A large negative bias over the cloudy area have been observed for both ABI-ALL and ABI-TH (Fig. 7). In addition, ABI-TH has higher negative mean prior biases (47%) and posterior biases (52%) compared to ABI-ALL (Table 4).

b. Impact on reflectivity and synthetic satellite forecasts

We assessed how assimilating all-sky radiance affected the reflectivity forecast by comparing simulated radar reflectivity against observed MRMS composite reflectivity. Forecasts initialized at 0000 UTC on 8 May 2020 showed that both the ABI-TH and CNTL experiments generated accurate 30-min, 60-min, and 90-min forecasts of the eastward-moving convection in northern Texas (Fig. 8), though the CNTL experiment performed better in terms of storm location. The ABI-ALL experiment performed significantly worse, as it failed to accurately forecast storm intensity and storm location. There were fewer differences among the three experiments for forecasts initialized at 2300 UTC on 21 June 2020 (Fig. 9). All three experiments correctly forecasted the evolution of convective cells over Kansas and produced few false alarms over the same region, though ABI-TH also correctly forecasted the evolution of the convective cells in Nebraska.

On 7 May 2021, ABI-ALL and ABI-TH accurately forecast a severe storm located on the western boarder of Texas in the southwestern portion of the domain. In addition, CNTL also generate the storm, but slightly displaced to the south to the MRMS observations (Fig. 10). This storm was depicted in both ABI-ALL and ABI-TH and persisted in those experiment until 0030 UTC. For the 23 May 2021 event, neither ABI-ALL nor CNTL accurately depicted convection in western South Dakota and along the Colorado-Nebraska border by 0030 UTC (Fig. 11), though ABI-TH began to forecast convection in this area. Qualitatively, the ABI-TH approach improved forecasts of convection on 7 May, 21 June 2020 and 23 May 2021, and the results were similar to the CNTL experiment. However, this assessment only represents a single forecast period for each event, and more quantitative analyses are needed to fully assess effects of all-sky radiance assimilation.

Fig. 12 shows ensemble mean-simulated WV69 brightness temperatures (K) at 0300 UTC in all three experiments, calculated from 3-hr forecasts initialized at 0000 UTC on 8 May 2020. The mid-level moisture environment and upper-level cloud forecasts were similar between ABI-TH and CNTL and associated with the supercells. In both ABI-TH and CNTL, forecasts of storm location and cloud coverage closely matched satellite observations, whereas the ABI-ALL forecasts predicted less moisture and a smaller area of cloud cover associated with the Texas-Oklahoma border supercell. All three experiments accurately forecasted the cold cloud top representation and the cloud-covered area for the far west Oklahoma convection. Each also produced similar forecasts for high temperature and associated dry areas that matched well with observations at the time. On 22 June 2020 at 0300 UTC, 3-hr forecasts from the ABI-ALL, ABI-TH, and CNTL experiments initialized at 0000 UTC showed similar moisture and cloud overage associated with the higher-end severe weather over south-central and central Kansas (Fig. 13). However, all three experiments underpredicted cloud cover and cloud temperature. On 8 May 2021 at 0300 UTC, the ABI-ALL and ABI-TH experiments performed better with respect to high-temperature dry lines, but underpredicted cloud top cold temperatures over the cloudy area to the southeast portion of the domain (Fig. 14). The WV69 values predicted for 0300 UTC from 3-hr forecasts showed several differences in forecasted cloud characteristics among the three experiments (Fig. 15).

c. Quantitative verification

We further assessed the overall performance of all-sky radiance assimilation experiments in the WoFS using an object-based verification method. The thresholds value used to identify radar reflectivity and rotation objects are similar to those used in Skinner et al. (2018). Observed rotation objects are defined as those where 2-5 km MRMS azimuthal shear is greater than 0.004 s^{-1}. While simulated rotation objects are defined as those where forecast 2-5 km UH is greater than 65 m^2s^{-2}. Observed reflectivity objects are defined by determining locations where simulated composite reflectivity is greater than 45 dBZ. The

MRMS objects are created using the same methods, but using a matched percentile threshold to model climatology (~41 dBZ). Table 5 lists the total number of reflectivity and rotation objects accumulated in the ABI-TH, ABI-ALL, and CNTL experiments as well as for each individual weather event. The ABI-ALL experiment generated a higher number of reflectivity objects for only the 7 May 2021 event; for the remaining three events, ABI-TH generated the most reflectivity objects. The CNTL experiment generated fewer reflectivity objects for all four events relative to the ABI assimilation methods. This is presumably because both the ABI-ALL and ABI-TH experiments generated higher biases of reflectivity and, consequently, a higher number of reflectivity objects, and hence more convection. On average, ABI-TH generated a higher total number of reflectivity and rotation objects across all four weather events. Only a few rotation objects were available for verification for the 7 May 20202 event, and the 21 June 2020 and 23 May 2021 events generated the largest number of reflectivity and rotation objects because they were associated with widespread convection.

Figures 16 and 17 show the 60-min, 90-min, and 120-min forecast performance for reflectivity and 2-5 km UH. For reflectivity, overall forecast skill was higher for the ABI-TH experiments relative to ABI-ALL. On 7 May 2020, the POD of ABI-TH was always higher, though the success ratio was very similar for the 60-min and 90-min forecasts (Fig. 16a-c). For the 120-min reflectivity forecast, ABI-TH showed the best performance among all experiments. The largest difference among experiments was for the 2-5 km UH forecast, where ABI-TH consistently performed best after 90 minutes (Fig. 17a-c). Interestingly, ABI-TH generated much higher UH skill for the 7 May 2020 case compared to ABI-ALL.

Among the reflectivity forecasts for 21 June 2020, ABI-ALL performed poorly at all forecast times, while the differences between the ABI-TH and CNTL experiments were generally small for both parameters. Forecast skill remained stable throughout the 120-min forecast period and decreased only slightly with time (Fig. 16d-f, Fig. 17d-f), showing POD values of more than 0.6 for reflectivity and 0.7 for UH. CSI values were between 0.3 and 0.5, and the success ratio was between 0.3 and 0.4, at all forecast times. For the 7 May 2021 event, ABI-TH performed better than the other two experiments in terms of the CSI values for reflectivity and UH (Fig. 16g-i, Fig. 17g-i). Overall, the quality of the UH forecast at all forecast times was poor for this event due to the unavailability of rotation data. The success ratios of composite reflectivity object forecast for both ABI-TH and CNTL were near 0.45, though ABI-TH had higher bias values and therefore a higher POD value.

For the 23 May 2021 event, reflectivity forecasts across all experiments were of acceptable quality, as evidenced by CSI values greater than 0.4 at all forecast times (Fig. 16j-l). The ABI-TH model performed better than ABI-ALL for the 60-min and 90-min forecasts (Fig. 16j, k), but CNTL performed best, especially for reflectivity at all forecast times. With respect to UH verification, CNTL consistently performed poorly at all forecast times and significantly worse than ABI-ALL and ABI-TH (Fig. 17j-l). However, forecast skill was stable within each experiment. Overall, the differing results between the reflectivity and UH verification forecasts highlight the poor performance of ABI-ALL relative to ABI-TH. The performance of ABI-TH was close to CNTL for most of the weather events considered by this study; specifically, the ABI-TH model performed better for UH forecasts on 7 May 2020 and 23 May 2021, but worse for reflectivity forecasts, relative to CNTL. Thus, our results collectively indicate that the forecast skill of ABI-TH is better than ABI-ALL but similar to CNTL.

4. Discussion and Conclusions

This study investigated the potential effects of assimilating adaptive-based, thinned GOES-16 data on forecasts of high-impact severe weather events by the WoFS. Our study moved beyond radiance assimilation to address the all-sky radiance data in the presence of clouds and precipitation in the WoFS, following Jones et al. (2020). Our results explore whether assimilating ABI all-sky radiance data from the GOES-16 water vapor channel, curated using adaptive-based data thinning techniques, can improve severe weather forecasts in the WoFS system. Most clear-sky data assimilation approaches reject observations affected by clouds, but these observations may contain valuable meteorological information. This study also aimed to extract more information from unobserved cloudy areas. Our results indicate that there are large, cloud-dependent negative biases over cloudy areas. In addition, assimilating all-sky radiance into the WoFS system produced similar results as assimilating only CWP data. One of the advantages of assimilating all-sky radiance data is the avoidance of uncertainties in the algorithm that retrieved the cloud properties. These retrieval algorithms differ from satellite to satellite and can be expensive and time-consuming (Derber and Wu, 1998). Directly assimilating cloud properties using all-sky radiance has its own advantages. For example, all-sky radiance provides unique observations that may be useful during convection initiation when they are assimilated alongside conventional and weather radar observations. To extract more usable information from high-resolution all-sky radiance data, more research is required on methods for bias correction, vertical and horizontal localization, and assimilation of multiple channels. In addition, future studies should investigate correlated observation errors using various assimilation systems. The present study examines forecast skill using all available daytime CWP and all-sky radiance data in the WoFS. Thus, the important question of assimilation of nighttime CWP and all-sky radiance data in the assimilation system, is not addressed in this work. Assimilation of nighttime data is important to know nighttime biases, error characteristics, and to use more data in the WoFS; however, we have deferred it for an independent study.

Acknowledgments:

We thank Dr. Nusrat Yussouf for careful internal review of this article at NSSL. This research was funded in part by the NOAA Warn-on-Forecast project. Additional funding was provided the under the NOAA-University of Oklahoma Cooperative Agreements NA16OAR4320115 and NA21OAR4320204, U.S. Department of Commerce. HRRRE initial and boundary conditions for this work were provided by the Global Systems Laboratory as part of real-time experiments in 2020 and 2021.

REFERENCES:

Aksoy, A., Dowell, D. and Snyder, C., 2009: A Multicase Comparative Assessment of the Ensemble Kalman Filter for Assimilation of Radar Observations. Part I: Storm-Scale Analyses. Mon. Wea. Rev., 137, 1805-1824. https://doi.org/10.1175/2008MWR2691.1

Auligné, T., and Wang, H., 2012: Assimilation of cloud-affected infrared satellite radiances. Abstract, 13th WRF Users' Workshop, Boulder, CO, UCAR, P13. [Available online at http://www2.mmm.ucar.edu/wrf/users/workshops/WS2012/abstracts/p13.htm.]

Barker, D. M., Huang, W., Guo, Y.-R., Bourgeois, A. J. and Xiao, Q. N., 2004: A three-dimensional variational data assimilation system for MM5: Implementation and initial results. Mon. Wea. Rev., 132, 897–914.

Berger, H., Forsythe, M., 2004: Satellite Wind Superobbing. Met Office Forecasting Research Technical Report, Met Office, Exeter UK, 451., Available: https://digital.nmla.metoffice.gov.uk/download/file/IO_ea4b7eb9-cac6-4519-9253-cdcddf38bdba

Bick, T., Simmer, C., Trömel, S., Wapler, K., Hendricks Franssen, H.-J., Stephan, K., Blahak, U., Schraff, C., Reich, H., Zeng, Y. and Potthast, R., 2016: Assimilation of 3D radar reflectivities with an ensemble Kalman filter on the convective scale. Q.J.R. Meteorol. Soc., 142: 1490–1504. doi: 10.1002/qj.2751.

Bonavita, M., Isaksen, L., and Hólm, E., 2012: On the use of EDA background error variances in the ECMWF 4 D-VAR. Quart. J. Roy. Meteor. Soc., 138, 1540–1559, https://doi.org/10.1002/qj.1899.

Bonavita, M., Hólm, E., Isaksen, L. and Fisher, M., 2016: The evolution of the ECMWF hybrid data assimilation system. Quart. J. Roy. Meteor. Soc., 142, 287–303, https://doi.org/10.1002/qj.2652.

Bormann, N., Lawrence, H., and Farnan, J, 2019: Global observing system experiments in the ECMWF assimilation system, ECMWF Technical Memoranda, Technical Memorandum No. 839, https://doi.org/10.21957/sr184iyz.

Chang, W., 2014: Convective-scale radar data assimilation and adaptive radar observation with the ensemble Kalman filter. Ph.D. thesis, McGill University, 154 pp., https://escholarship.mcgill.ca/concern/theses/8s45qc87q

Clayton, A. M., Lorenc, A. C., and Barker, D. M., 2013: Operational implementation of a hybrid ensemble/4 D-VAR global data assimilation system at the Met Office. Quart. J. Roy. Meteor. Soc., 139, 1445–1461, https://doi.org/10.1002/qj.2054.

Courtier, P., and Talagrand, O., 1987: Variational assimilation of meteorological observations with the adjoint vorticity equation. Part II: Numerical results. Quart. J. Roy. Meteor. Soc., 113, 1329–1347.

Derber, J. C., and Wu, W., 1998: The Use of TOVS Cloud-Cleared Radiances in the NCEP SSI Analysis System. Mon. Wea. Rev., 126, 8, 2287-2299, <https://doi.org/10.1175/1520-0493(1998)126<2287:TUOTCC>2.0.CO;2>

Developmental Testbed Center, 2017: Gridpoint Statistical Interpolation Advanced User's Guide Version 3.6.0.0. Available at http://www.dtcenter.org/com-GSI/users/docs/index.php, 143 pp.

Dowell, D. C., Wicker, L. J. and Snyder, C., 2011: Ensemble Kalman filter assimilation of radar observations of the 8 May 2003 Oklahoma City supercell: Influences of reflectivity observations on storm-scale analyses. Mon. Wea. Rev., 139, 272–294, doi: 10.1175/2010MWR3438.1.

Fischer, C., Montmerle, T., Berre, L., Auger, L., and Stefanescu, S. E., 2005: An overview of the variational assimilation in the ALADIN/France numerical weather-prediction system. Q. J. R. Met. Soc. 131, 3477–3492. doi: 10.1256/qj.05.115

Geer, A. J., and Bauer, P., 2011: Observation errors in all-sky data assimilation. Quart. J. Roy. Meteor. Soc., 137, 2024–2037, doi:10.1002/qj.830.

Geer, A., Baordo, F., Bormann, N., Chambon, P., English, S., Kazumori, M., Lawrence, H., Lean, P., Lonitz, K., and Lupu, C., 2017: The growing impact of satellite observations sensitive to humidity, cloud and precipitation, Q. J. R. Meteorol. Soc., 143, 3189–3206., https://doi.org/10.1002/qj.3172.

Geer, A. J., Coauthors, 2018: All-sky satellite data assimilation at operational weather forecasting centres. Q.J.R. Meteorol. Soc., 144, 1191–1217, doi:10.1002/qj.3202.

Geer, A. J., Matricardi, M., and Migliorini, S., 2019: All-sky assimilation of infrared radiances sensitive to mid- and upper-tropospheric moisture and cloud, Atmospheric Measurement Techniques, 12, 4903–4929, doi:10.5194/amt-12-4903-2019.

George, J. P., and Coauthors, 2016: NCUM Data Assimilation System. Technical Report NMRF/TR/01/2016. National Centre for Medium Range Weather Forecasting (NCMRWF), Noida, India. 21 pp.

Gregow, E., Lindfors, A.V., van der Veen, S.H., Schoenach, D., de Haan, S., Lindskog, M., 2020: The use of satellite and surface observations for initializing clouds in the HARMONIE NWP model. Meteorol Appl.;27:e1965. https://doi.org/10.1002/met.1965

Han, Y., Weng, F., Liu, Q., and van Delst, P., 2007: A fast radiative transfer model for SSMIS upper atmosphere sounding channels. J. Geophys. Res., 112, D11121, doi:10.1029/2006JD008208.

Honda, T., and Coauthors, 2018: Assimilating all-sky Himawari-8 infrared radiances: A case of Typhoon Soudelor (2015). Mon. Wea. Rev., 146, 213–229, https://doi.org/10.1175/MWR-D-16-0357.1.

Hu, M., Xue, M. and Brewster, K., 2006: 3DVAR and cloud analysis with WSR-88D level-II data for the prediction of the Fort Worth, Texas, tornadic thunderstorms. Part I: Cloud analysis and its impact. Mon. Wea. Rev.,134, 675–698, doi:10.1175/MWR3092.

Janjic ́, T., and Coauthors, 2018: On the representation error in data assimilation. Quart. J. Roy. Meteor. Soc., 144, 1257–1278, https://doi.org/10.1002/qj.3130.

Jolliffe, I. T., and Stephenson, D. B., 2003: Forecast Verification: A Practitioner’s Guide in Atmospheric Science. John Wiley and Sons, 254 pp.

Kazumori, Masahiro, 2014: Satellite Radiance Assimilation in the JMA Operational Mesoscale 4DVAR System. Mon. Wea. Rev., 142.3, 361-1381. https://doi.org/10.1175/MWR-D-13-00135.1

Jones, T.A. and Stensrud, D.J., 2015: Assimilating Cloud Water Path as a Function of Model Cloud Microphysics in an Idealized Simulation. Mon. Wea. Rev., 143, 2052–2081, https://doi.org/10.1175/MWR-D-14-00266.1

Jones, T.A., Knopfmeier, K., Wheatley, D., Creager, G., Minnis, P., Palikonda, R., 2016. Storm-scale data assimilation and ensemble forecasting with the NSSL experimental warn on-forecast system. Part I: combined radar and satellite assimilation. Wea. Forecast. 31, 297–327. https://doi.org/10.1175/WAF-D-15-0107.1.

Jones, T.A., Skinner, P., Knopfmeier, K., Mansell, E., Minnis, P., Palikonda, R., Smith, W., 2018a. Comparison of cloud microphysics schemes in a warn-on-forecast system using synthetic satellite objects. Wea. Forecast. 33, 1681–1708. https://doi.org/10. 1175/WAF-D-18-0112.1.

Jones, T.A., Wang, X., Skinner, P., Johnson, A., Wang, Y., 2018b. Assimilation of GOES-13 Imager clear-sky water vapor (6.5 mm) radiances into a Warn-on-Forecast system. Mon. Wea. Rev. 146, 1077–1107. https://doi.org/10.1175/MWR-D-17-0280.1.

Jones, T.A., Skinner, P., Yussouf, N., Knopfmeier, K., Reinhart, A., Dowell, D., 2019. Forecasting high-impact weather in landfalling tropical cyclones using a warn-on- forecast system. Bull. Amer. Meteor. Soc. 100, 1405–1417. https://doi.org/10.1175/ BAMS-D-18-0203.1.

Jones, T. A., Skinner, P., Yussouf, N., Knopfmeier, K., Reinhart, A., Wang, X., Bedka, K., Smith, W., Jr., and Palikonda, R., 2020. Assimilation of GOES-16 Radiances and Retrievals into the Warn-on-Forecast System. Mon Wea Rev 148, 5, 1829-1859, https://doi.org/10.1175/MWR-D-19-0379.1

Kerr, C. A., and Wang, X., 2020: Ensemble-based targeted observation method applied to radar radial velocity observations on idealized supercell low-level rotation forecasts: A proof of concept. Mon. Wea. Rev., 148, 877–890, https://doi.org/10.1175/ MWR-D-19-0197.1.

Kerr, C. A., Wicker, L. J., and Skinner, P. S., 2021: Updraft-Based Adaptive Assimilation of Radial Velocity Observations in a Warn-on-Forecast System. Weather and Forecasting 36, 1, 21-37, available from: < https://doi.org/10.1175/WAF-D-19-0251.1>

Kidder, S. Q., and Vonder Haar, T. H., 1995: Satellite Meteorology, Page 53, (San Diego: Academic Press).

Kleist, D. T., and Ide, K., 2015: An OSSE-based evaluation of hybrid variational–ensemble data assimilation for the NCEP GFS. Part II: 4DEnVar and hybrid variants. Mon. Wea. Rev., 143, 452–470, https://doi.org/10.1175/MWR-D-13-00350.1.

Klinker, E., Rabier, F., Kelly, G., and Mahfouf, J-F., 2000: The ECMWF operational implementation of four-dimensional variational assimilation. III: Experimental results and diagnostics with operational configuration. Quart. J. Roy. Meteor. Soc., 126, 1191–1215.

Lábó, Eszter, Kerényi, J., and Putsay, M., 2007: The parallax correction of MSG images on the basis of the SAFNWC cloud top height product. Proceedings EUMETSAT Meteorological Satellite Conf. and 15th Satellite Meteorology and Oceanography Conf. Amer. Meteor. Soc., Amsterdam, the Netherlands.

Lawson, J. R., and Coauthors, 2018: Advancing from Convection-Allowing NWP to Warn-on-Forecast: Evidence of Progress, Weather and Forecasting 33, 2: 599-607, https://doi.org/10.1175/WAF-D-17-0145.1

Lei, L., Wang, Z., and Tan, Z., 2021: Integrated Hybrid Data Assimilation for an Ensemble Kalman Filter. Monthly Weather Review 149, 12, 4091-4105, https://doi.org/10.1175/MWR-D-21-0002.1

Li, J., and Coauthors, 2021: Satellite all-sky infrared radiance assimilation: Recent progress and future perspectives. Adv. Atmos. Sci., https://doi.org/10.1007/s00376-021-1088-9.

Liu, Z. Q. and Rabier, F., 2002: The interaction between model resolution, observation resolution and observation density in data assimilation: A one-dimensional study. Q. J. R. Meteorol. Soc., 128, 1367-1386.

Liu, Z., Schwartz, C.S., Snyder, C., and Ha, S. Y., 2012: Impact of assimilating AMSU-A radiances on forecasts of 2008 Atlantic tropical cyclones initialized with a limited-area ensemble Kalman filter. Mon. Wea. Rev., 140, 4017–4034, doi:10.1175/MWR-D-12-00083.1.

Lu, H., and Xu, Q., 2009: Trade-Offs between Measurement Accuracy and Resolutions in Configuring Phased-Array Radar Velocity Scans for Ensemble-Based Storm-Scale Data Assimilation. Journal of Applied Meteorology and Climatology, 48, 6, 1230-1244, https://doi.org/10.1175/2008JAMC2009.1

Lu, X., and Wang, X., 2021: Improving the Four-Dimensional Incremental Analysis Update (4DIAU) with the HWRF 4DEnVar Data Assimilation System for Rapidly Evolving Hurricane Prediction. Monthly Weather Review 149, 12, 4027-4043, https://doi.org/10.1175/MWR-D-21-0068.1

Majcen, M., Markowski, P., Richardson, Y., Dowell, D., and Wurman, J., 2008: Multipass objective analyses of Doppler radar data. J. Atmos. Oceanic Technol., 25, 1845 1858, https://doi.org/10.1175/2008JTECHA1089.1.

Mallick, S., Indira Rani, S., Srinivas, D., and George, J.P., 2016: Assimilation of CrIS hyperspectral radiances in a 4D-VAR assimilation system. Proc. SPIE 9880, Multispectral, Hyperspectral, and Ultraspectral Remote Sensing Technology, Techniques and Applications VI, 98800Q, New Delhi, India, doi: 10.1117/12.2222775.

Mallick, S., Dutta, D., and Min, K.-H., 2017: Quality assessment and forecast sensitivity of global remote sensing observations. Adv. Atmos. Sci., 34(3), 371–382, doi:10.1007/s00376-016-6109-8.

Mallick, S., and Jones, T. A., 2020: Assimilation of GOES-16 satellite derived winds into the warn-on-forecast system. Atmospheric Research, 245, 105131. https://doi.org/10.1016/j.atmosres.2020.105131

Mansell, E.R., Ziegler, C.L., and Bruning, E.C., 2010: Simulated Electrification of a Small Thunderstorm with Two-Moment Bulk Microphysics. J. Atmos. Sci., 67, 171–194,https://doi.org/10.1175/2009JAS2965.1

Matricardi, M., Chevallier F. , , Kelly G. , , and Thepaut J.-N. , 2004: An improved general fast radiative transfer model for the assimilation of radiance observations. Quart. J. Roy. Meteor. Soc., 130, 153–173, doi:10.1256/qj.02.181.

McNally, A., 2009: The direct assimilation of cloud-affected satellite infrared radiances in the ECMWF 4DVar. Q. J. R. Meteorol. Soc., 135, 1214-1229.

McNally, A., 2014: The Impact of Satellite Data on NWP. ECMWF Seminar on Use of Satellite Observations in NWP, Reading, United Kingdom, 8-12 September 2014, 1-10. https://www.ecmwf.int/sites/default/files/elibrary/2015/11061-impact-satellite-data-nwp.pdf

Minamide, M., and Zhang, F., 2017: Adaptive Observation Error Inflation for Assimilating All-Sky Satellite Radiance, Mon. Wea. Rev, 145(3), 1063-1081.

Minnis, P., and Coauthors, 2011: CERES Edition-2 cloud property retrievals using TRMM VIRS and Terra and Aqua MODIS data, Part I: Algorithms. IEEE Trans. Geosci. Remote Sens., 49, 4374–4400, doi:https://doi.org/10.1109/TGRS.2011.2144601.

Ochotta, T., Gebhardt, C., Saupe, D., and Wergen, W., 2005: Adaptive thinning of atmospheric observations in data assimilation with vector quantization and filtering methods. Quart. J. Roy. Meteor. Soc., 131, 3427–3437, https://doi.org/10.1256/qj.05.94.

Otkin, J. A., 2012: Assimilation of water vapor sensitive infrared brightness temperature observations during a high impact weather event. J. Geophys. Res., 117, D19203, doi:10.1029/ 2012JD017568.

Pan, Y., Zhu, K., Xue, M., Wang, X., Hu, M., Benjamin, S. G., Weygandt, S. S., & Whitaker, J. S., 2014: A GSI-Based Coupled EnSRF–En3DVar Hybrid Data Assimilation System for the Operational Rapid Refresh Model: Tests at a Reduced Resolution, Mon. Wea. Rev., 142(10), 3756-3780., doi:10.1175/MWR-D-13-00242.1

Pangaud, T., Fourrie, N., Guidard, V., Dahoui, M., & Rabier, F., 2009: Assimilation of AIRS Radiances Affected by Mid- to Low-Level Clouds. Mon. Wea. Rev., 137, 4276-4292.

Penny, S. G., 2014: The hybrid local ensemble transform Kalman filter. Mon. Wea. Rev., 142, 2139–2149, https://doi.org/10.1175/MWR-D-13-00131.1.

Rawlins, F., and Coauthors, 2007: The Met Office global four-dimensional variational data assimilation scheme. Quart. J. Roy. Meteor. Soc., 133, 347–362.

Reale, O., and Coauthors, 2018: Impact of Adaptively Thinned AIRS Cloud-Cleared Radiances on Tropical Cyclone Representation in a Global Data Assimilation and Forecast System. Weather and Forecasting 33, 4, 909-931, https://doi.org/10.1175/WAF-D-17-0175.1

Roebber, P.J., 2009: Visualizing multiple measures of forecast quality. Wea. Forecasting, 24, 601–608, https://doi.org/10.1175/2008WAF2222159.1.

Salonen, K., and Coauthors, 2009: Doppler radar radial winds in HIRLAM. Part II: Optimizing the super-observation processing. Tellus, 61A, 288–295, https://doi.org/10.1111/j.1600-0870.2008.00381.x.

Saunders, R., Matricardi, M., and Brunel, P., 1999: An improved fast radiative transfer model for assimilation of satellite radiance observations. Quart. J. Roy. Meteor. Soc., 125, 1407–1425, doi:10.1002/qj.1999.49712555615.

Saunders, R., and Coauthors 2018: An update on the RTTOV fast radiative transfer model (currently at version 12), Geosci. Model Dev., 11, 2717–2737, https://doi.org/10.5194/gmd-11-2717-2018.

Schmit, T. J., Gunshor, M. M., Menzel, W. P., Gurka, J. J., Li, J., and Bachmeier, A. S. 2005: Introducing the next-generation Advanced Baseline Imager (ABI) on GOES-R. Bull. Amer. Meteor. Soc., 86, 1079–1096, doi:10.1175/BAMS-86-8-1079.

Schmit, T. J., Griffith, P., Gunshor, M. M., Daniels, J. M., Goodman, S. J., and Lebair, W. J., 2017: A Closer Look at the ABI on the GOES-R Series. Bull. Amer. Meteor. Soc., 98 (4), 681-698, https://doi.org/10.1175/BAMS-D-15-00230.1

Sharma, P., Indira Rani, S., Mallick, S., Srinivas, D., George, J. P., and Dasgupta,M., 2016: IASI hyperspectral radiances in the NCMRWF 4D-VAR assimilation system: OSE. Proc.

SPIE 9880, Multispectral, Hyperspectral, and Ultraspectral Remote Sensing Technology, Techniques and Applications VI, 98800P, New Delhi, India, doi: 10.1117/12.2225868.

Shi X K, Li, Y D, Liu, J W, Xiang, X Z, and Liu, L., 2018. Simulation of FY-2D infrared brightness temperature and sensitivity analysis to the errors of WRF simulated cloud variables. Science China Earth Sciences, 61: 957–972, https://doi.org/10.1007/s11430-017-9150-0

Skamarock, W. C., and Coauthors, 2008: A description of the Advanced Research WRF version 3. NCAR Tech. Note NCAR/TN-4751STR, 113 pp., https://dx.doi.org/10.5065/D68S4MVH. fA

Skinner, P.S., Wicker, L.J., Wheatley, D.M. and Knopfmeier, K.H., 2016: Application of Two Spatial Verification Methods to Ensemble Forecasts of Low-Level Rotation. Wea. Forecasting, 31, 713–735, https://doi.org/10.1175/WAF-D-15-0129.1

Skinner, P. S., Wheatley, D. M., Knopfmeier, K. H., Reinhart, A. E., Choate, J. J., Jones, T. A., Creager, G. J., Dowell, D. C., Alexander, C. R., Ladwig, T. T., Wicker, L. J., Heinselman, P. L., Minnis, P., and Palikonda, R., 2018: Object-Based Verification of a Prototype Warn-on-Forecast System. Wea. Forecasting, 33, 1225–1250, https://doi.org/10.1175/WAF-D-18-0020.1

Smith, T. M., and Coauthors, 2016: Multi-Radar Multi-Sensor (MRMS) severe weather and aviation products: Initial operating capabilities. Bull. Amer. Meteor. Soc., 97, 1617–1630, https://doi.org/10.1175/BAMS-D-14-00173.1.

Srinivas, D., Indira Rani, S., Mallick, S., George, J. P., and Sharma, P., 2016: Impact of AIRS radiance in the NCUM 4D-VAR assimilation system. Proc. SPIE 9880, Multispectral, Hyperspectral, and Ultraspectral Remote Sensing Technol ogy, Techniques and Applications VI, 98800O, New Delhi, India, doi: 10.1117/12.2223516.

Snyder, C., and Zhang, F., 2003: Assimilation of simulated Doppler radar observations with an ensemble Kalman filter. Mon. Wea. Rev., 131, 1663–1677, doi:10.1175//2555.1

Sun, J., and Wang, H., 2013: Radar Data Assimilation with WRF 4D-Var. Part II: Comparison with 3D-Var for a Squall Line over the U.S. Great Plains. Monthly Weather Review 141, 7, 2245-2264, https://doi.org/10.1175/MWR-D-12-00169.1

Tanguay, M., Fillion, L., Lapalme, E., and Lajoie, M., 2012: Four-Dimensional Variational Data Assimilation for the Canadian Regional Deterministic Prediction System. Monthly Weather Review 140, 5, 1517-1538, https://doi.org/10.1175/MWR-D-11-00160.1

Tavolato, C., and Isaksen, L., 2015: On the use of a Huber norm for observation quality control in the ECMWF 4D-Var. Quart. J. Roy. Meteor. Soc., 141, 1514–1527, doi:10.1002/qj.2440.

Thepaut, J.-N., 2003: Satellite data assimilation in numerical weather prediction: An overview. Proceedings of ECMWF Seminar on Recent Developments in Data Assimilation for Atmosphere and Ocean, ECMWF, Reading, UK 8-12 September 2003, 75-96.

Tong, M., Sippel, J. A., Tallapragada, V., Liu, E., Kieu, C., Kwon, I., Wang, W., Liu, Q., Ling, Y., & Zhang, B., 2018: Impact of assimilating aircraft reconnaissance observations on tropical cyclone initialization and prediction using operational HWRF and GSI ensemble–variational hybrid data assimilation. Mon. Wea. Rev., 146, 4155–4177, https://doi.org/10.1175/MWR-D-17-0380.1.

Wang, C., and Huang, X., 2014: Parallax correction in the analysis of multiple satellite data sets. IEEE Geosci. Remote Sens. Lett., 11, 965–969, https://doi.org/10.1109/LGRS.2013.2283573.

Wang, Y., Yussouf, N., Mansell, E. R., Matilla, B. C., Kong, R., Xue, M., and Chmielewski, V. C., 2021: Impact of Assimilating GOES-R Geostationary Lightning Mapper Flash Extent Density Data on Severe Convection Forecasts in a Warn-on-Forecast System. Monthly Weather Review 149, 10, 3217-3241, https://doi.org/10.1175/MWR-D-20-0406.1

Weng, F., 2007: Advances in radiative transfer modeling in support of satellite data assimilation. J. Atmos. Sci., 64, 3799–3807, doi:10.1175/2007JAS2112.1.

Wheatley, D. M., Knopfmeier, K. H., Jones, T. A., & Creager, G. J., 2015: Storm-scale data assimilation and ensemble forecasting with the NSSL Experimental Warn-on-Forecast System. Part I: Radar data experiments. Wea. Forecasting, 30, 1795–1817, https://doi.org/10.1175/WAF-D-15-0043.1.

Whitaker, J. S., and Hamill, T. M., 2002: Ensemble data assimilation without perturbed observations. Mon. Wea. Rev., 130, 1913–1924.

Xu, D., Liu, Z., Huang, X.-Y., Min, J., and Wang, H., 2013: Impact of assimilating IASI radiance observations on forecasts of two tropical cyclones. Meteor. Atmos. Phys., 122, 1–18, doi:10.1007/s00703-013-0276-2.

Yang, C., Z. Liu, F. Gao, P. P. Childs, and J. Min, 2017, Impact of assimilating GOES imager clear-sky radiance with a rapid refresh assimilation system for convection-permitting forecast over Mexico, J. Geophys. Res. Atmos., 122, 5472–5490, doi:10.1002/2016JD026436.

Zhang, Y., Zhang, F., and Stensrud, D. J., 2018: Assimilating All-Sky Infrared Radiances from GOES-16 ABI Using an Ensemble Kalman Filter for Convection-Allowing Severe Thunderstorms Prediction. Monthly Weather Review 146, 10, 3363-3381, https://doi.org/10.1175/MWR-D-18-0062.1

Zhu, Y., Liu, E., Mahajan, R., Thomas, C., Groff, D., Van Delst, P., Collard, A., Kleist, D., Treadon, R., and Derber, J. C., 2016: All-sky microwave radiance assimilation in the NCEP's GSI analysis system. Mon. Weather Rev. 144: 4709–4735. http://dx.doi.org/10.1175/MWR-D-15-0445.1.

Zou, X., Zhuge, X., and Weng, F., 2016. Characterization of Bias of Advanced Himawari Imager Infrared Observations from NWP Background Simulations Using CRTM and RTTOV. Journal of Atmospheric and Oceanic Technology 33, 12, 2553-2567, <https://doi.org/10.1175/JTECH-D-16-0105.1>

Table 1: List of the observation type, horizontal and vertical covariance localization length scale and the observations error used by the WoFS system. Vertical localization radii are given in units of scale height (SH). For cloudy regions, WV73 errors are double to account for larger uncertainties in these measurements and are similar to those used by Jones et al. (2020).

Observation Type	Variables	Horizontal localization (km)	Vertical Localization (SH)	Observation Error
Mesonet and ASOS	Eastward (*u*-) wind	60-460	0.85	1.75 m s $^{-1}$
	Northward (*v*-) wind	60-460	0.85	1.75 m s $^{-1}$
	Temperature	60-460	0.85	1.75 K
	Dewpoint	60-460	0.85	2.0 K

	Pressure	60-460	0.85	1.0 hPa
Radar	Reflectivity	18	0.8	7.0 dBZ
	Radial velocity	18	0.8	3.0 m s^{-1}
Satellite (GOES-16)	CWP	36	0.9	0.025 - 0.2 kg m^{-2}
	ABI-WV62	36	4.0	1.25 (K)
	ABI-WV73	36	4.0	1.75 (K)

Table 2. Total number of tornado, severe hail (diameter > 1.0 in.), and high-wind reports within the model domain for each case consider in this study. The total number is counted over the study domain between the time 1800 and 0500 UTC the following day.

Event	Tornadoes	Hail	Wind
7 MAY, 2020	0	79	76
21 JUNE, 2020	6	49	81
7 MAY, 2021	0	3	17
23 MAY, 2021	14	18	50

Table 3. Summary of total number of observations assimilated.

Event	ABI-TH	ABI-ALL	CNTL
7 MAY, 2020	234991	427351	406804
21 JUNE, 2020	125105	261066	386996
7 MAY, 2021	199011	288840	104985
23 MAY, 2021	192544	490280	380743

Table 4. Prior (*O-B*) and posterior biases (*O-A*) averaged overall assimilation cycles for each case 4 different experiments.

Experiment	7 MAY, 2020		21 JUNE, 2020		7 MAY, 2021		23 MAY, 2021	
	O-B	*O-A*	*O-B*	*O-A*	*O-B*	*O-A*	*O-B*	*O-A*
ABI-TH (K)	-1.72	-1.41	-5.57	-3.14	-0.45	-0.33	-1.94	-1.44
ABI-ALL (K)	-1.59	-1.30	-3.41	-1.97	-0.44	-0.29	-1.02	-0.69
CNTL (kg m $^{-2}$)	0.37	0.33	0.35	0.27	0.23	0.21	0.18	0.15

Table 5. Summary of total number of reflectivity and rotation objects accumulated over all the ensemble member and 180-min forecasts times for all four cases.

	Event -->	7 MAY, 2020	21 JUNE, 2020	7 MAY, 2021	23 MAY, 2021
dBZ	ABI-TH	75669	150670	66768	148498
	ABI-ALL	68882	136894	70140	145410
	CNTL	67849	137577	57661	123711
Rotation	ABI-TH	38469	58321	8161	49880
	ABI-ALL	39052	54151	8272	45552
	CNTL	42289	57617	9277	43683

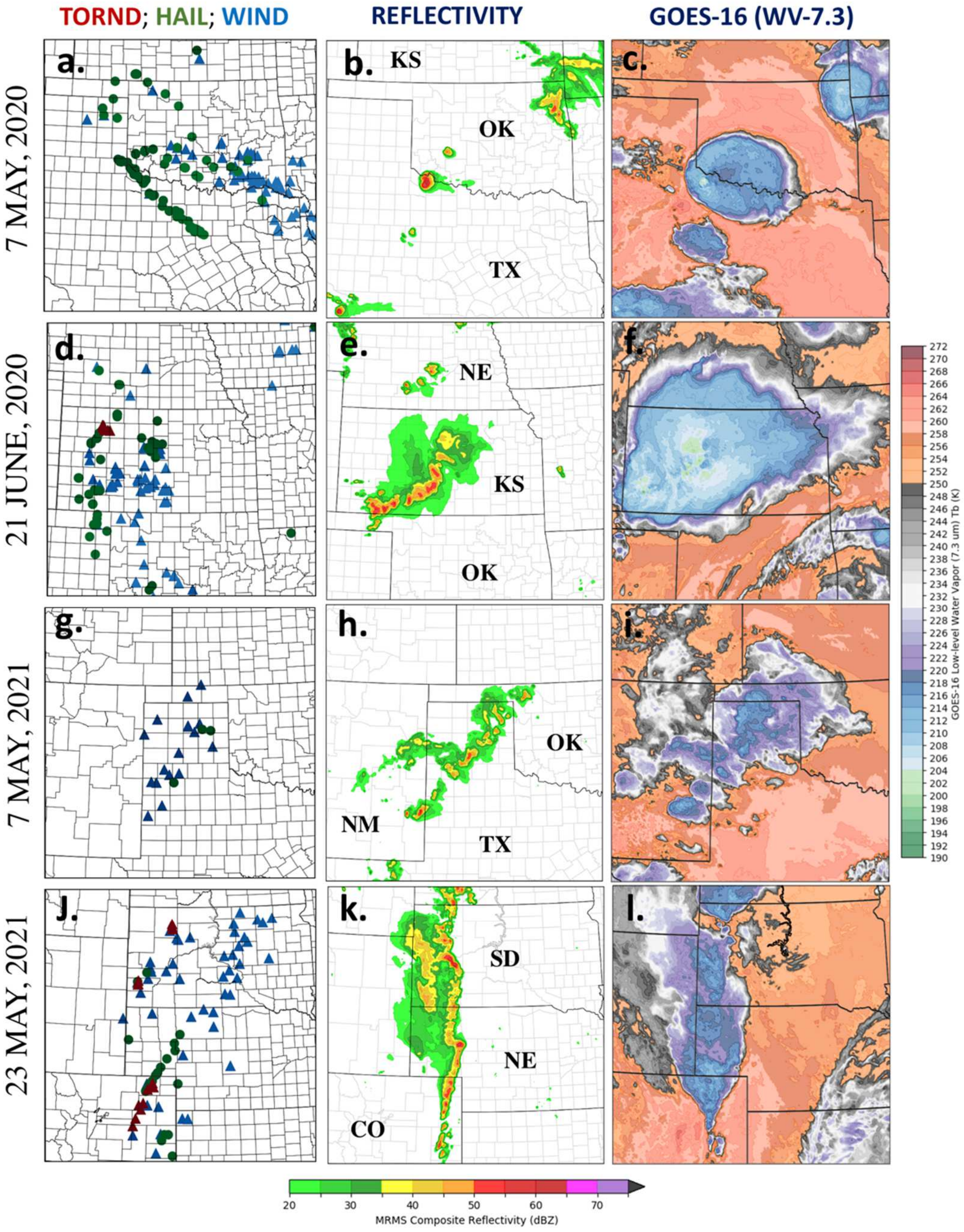

Figure 1: Location of tornado (triangle), hail (circle) and wind (triangle) reports, MRMS composite reflectivity (dBZ) and GOES-16 low level WV (7.3 μm) at 0000 UTC analysis time for each event over the model domain.

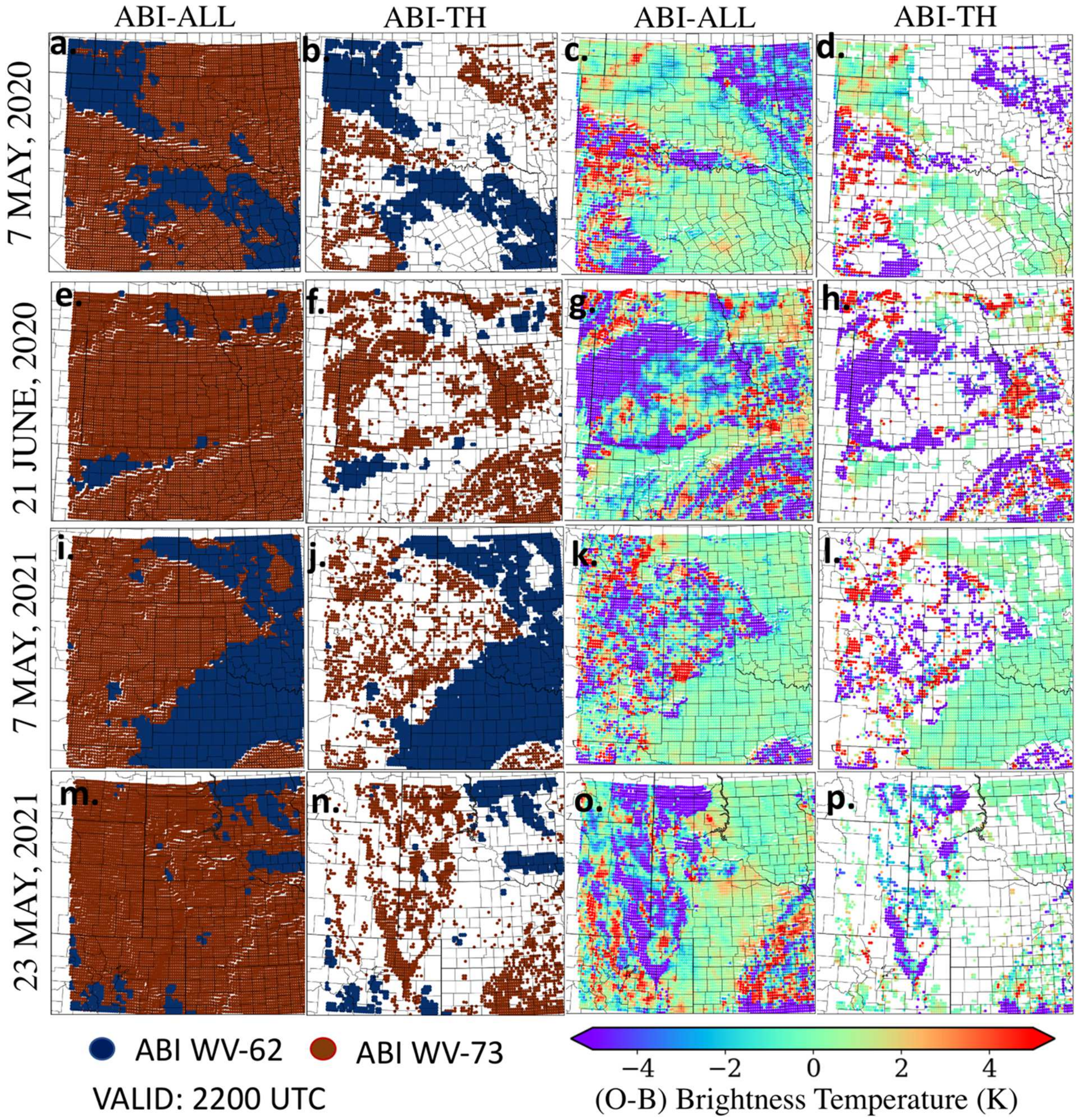

Figure 2: Spatial distribution of 2200 UTC assimilated GOES-16 water vapor 6.2 μm (blue circle) and 7.3 μm (red circle) brightness temperature location with adaptive data thinning method (ABI-TH) and with all available data within the study domain of each case. The corresponding (*O-B*) brightness temperate difference (K) are also shown in the right panels and are valid at the same time.

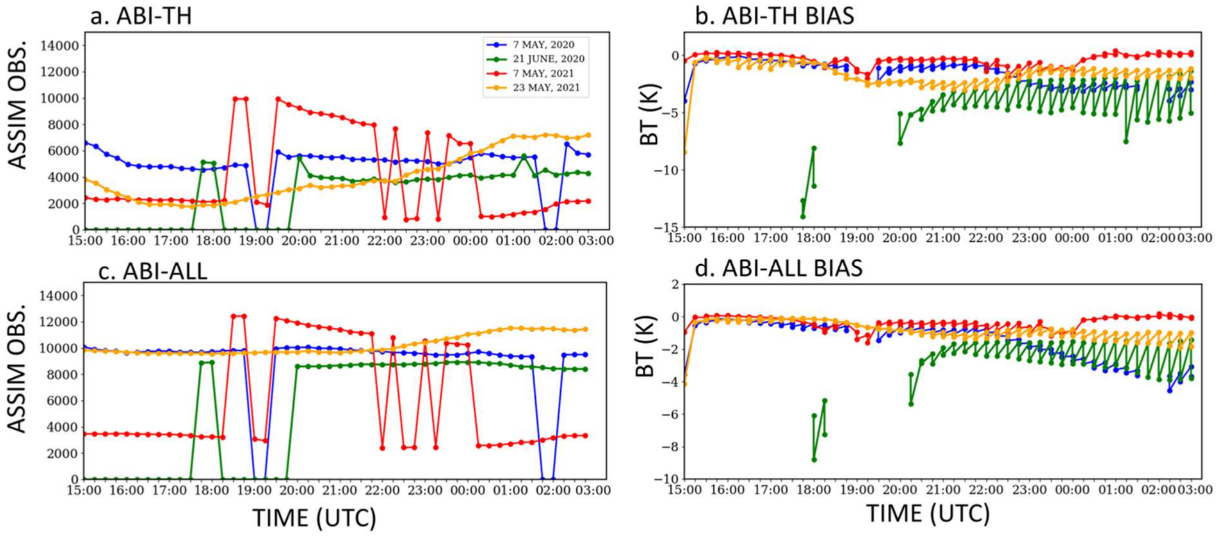

Figure 3: Number of (a.) thinned all-sky ABI and (c) all available all-sky ABI observations assimilated in GSI-EnKF based WoFS system. Mean prior and posterior innovations (*O-B, O-A*) for (b.) thinned all-sky ABI observation and (d.) all available all-sky ABI at 15 min assimilation cycle from 1500 UTC to next day 0300 UTC. Note that for the 21 June, 2020 case the assimilation period starts at 1800 UTC.

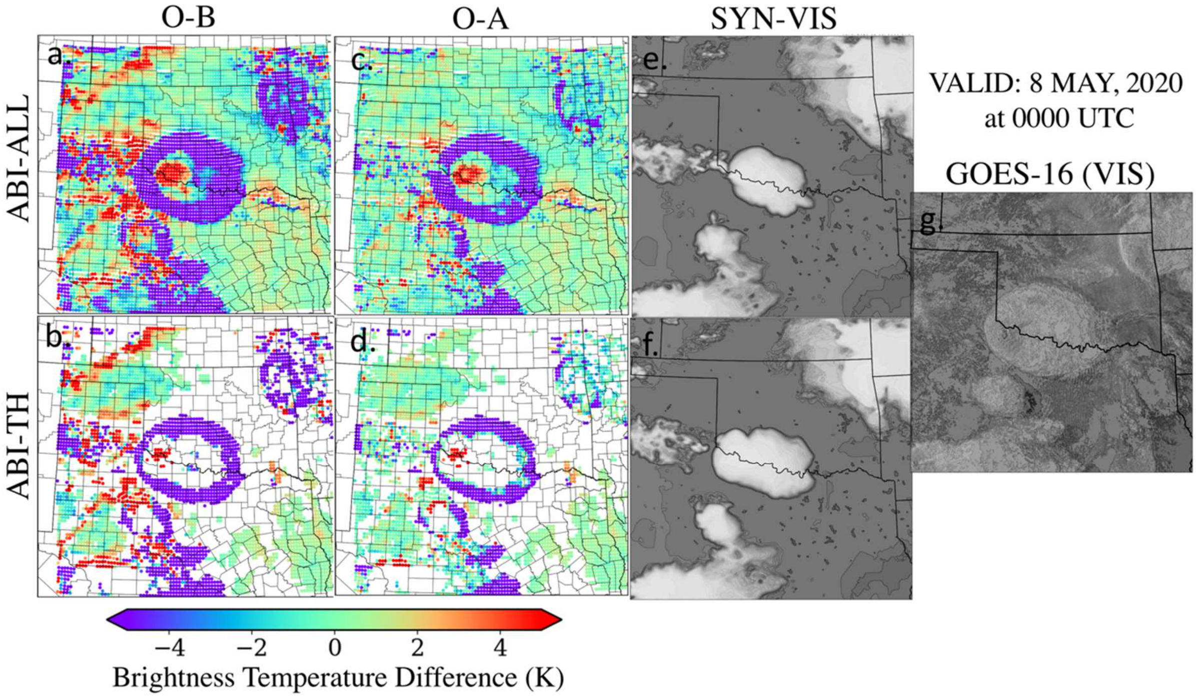

Figure 4: Differences between observations and simulated BT of all assimilated ABI channels of prior mean (*O-B*) and posterior mean (*O-A*) of EnKF. The synthetic visible observation created using two type of experiment all are valid at 0000 UTC on 8 May 2020.

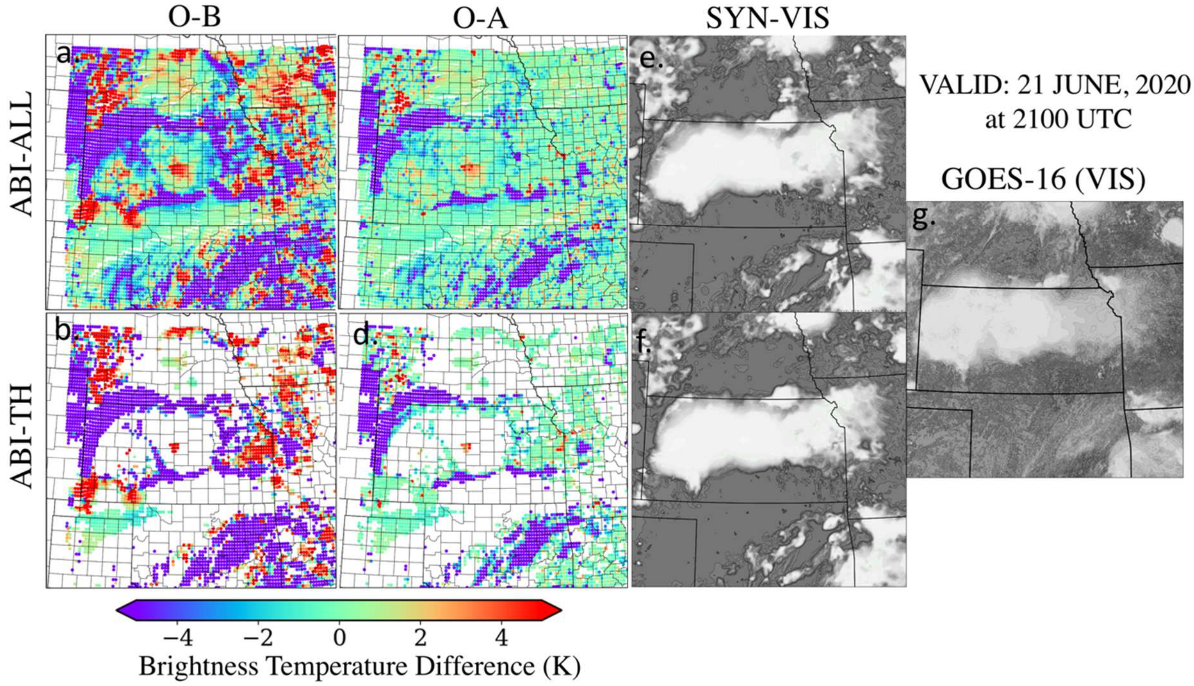

Figure 5. Same as Figure 4. but for 21 June, 2020 event valid at 2100 UTC.

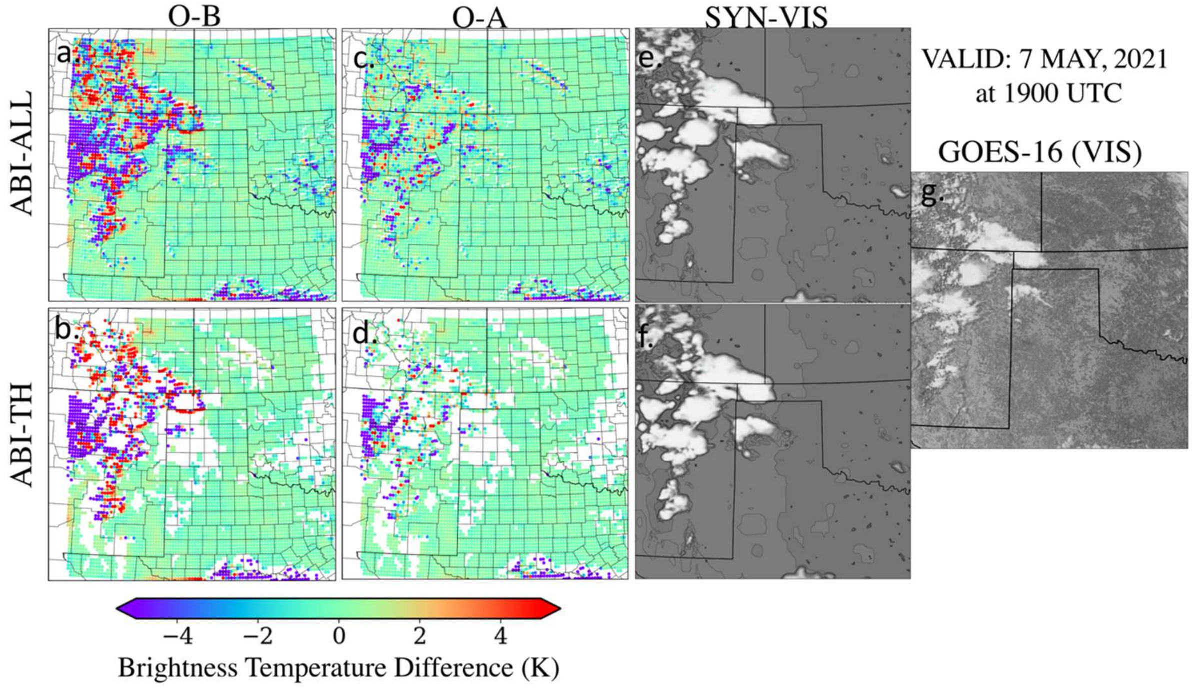

Figure 6. Same as Figure 4. but for 7 may, 2021 event valid at 1900 UTC.

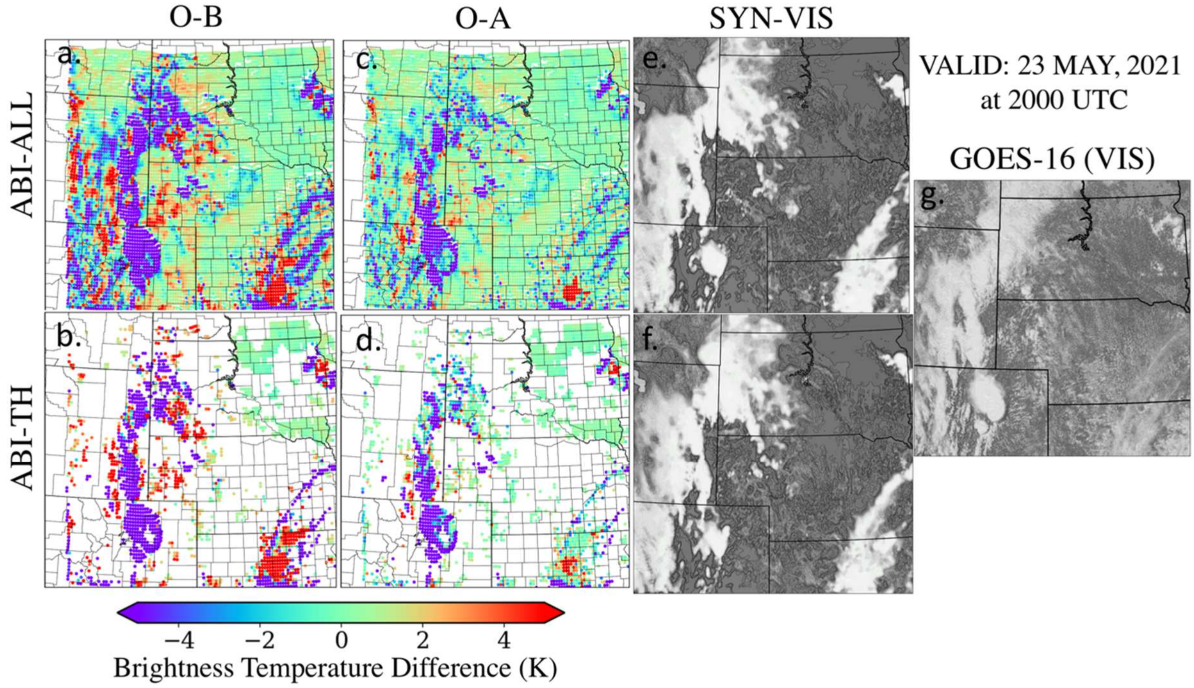

Figure 7. Same as Figure 4. but for 23 may, 2021 event valid at 2300 UTC.

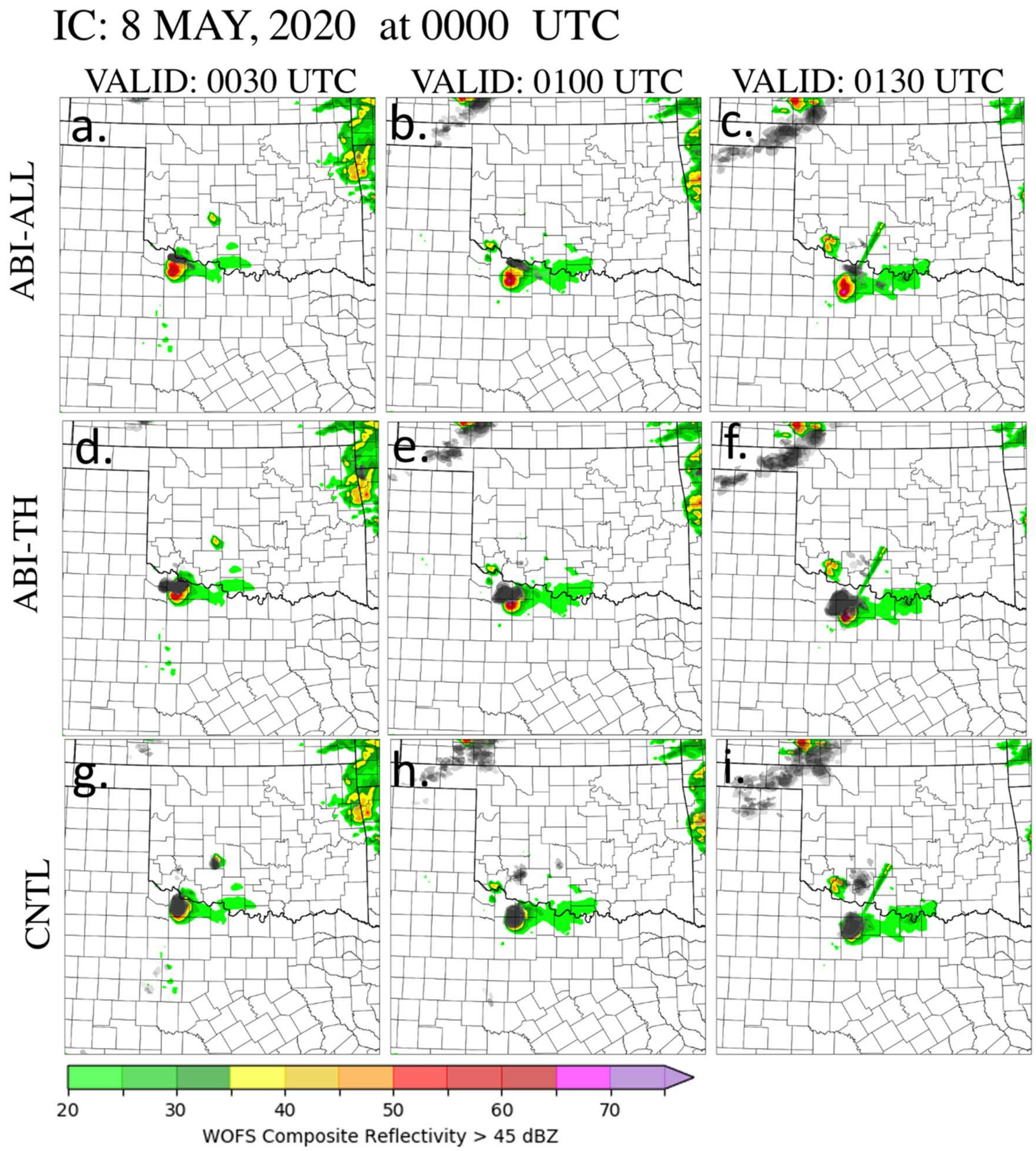

Figure 8: Forecast composite reflectivity > 45 dBZ from ABI-TH2K, ABI-ALL, and CNTL initiated at 0000 UTC 8 May, 2020 for each experiment. Darker grays indicate more members generate convection at a particular location. Background plot shows MRMS composite reflectivity valid at the forecast time.

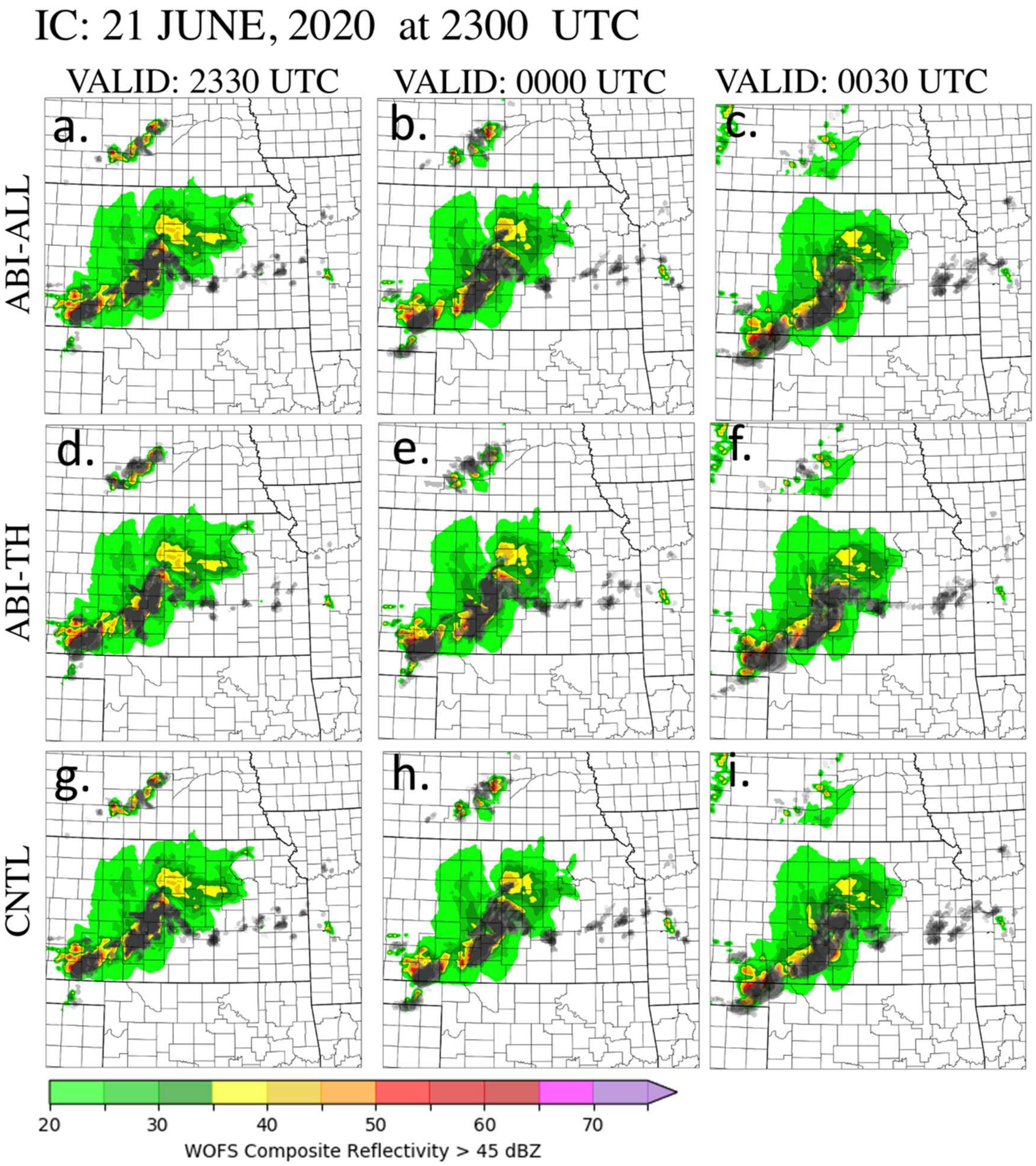

Figure 9. Same as Figure 8. but for reflectivity forecasts initialize at 2300 UTC 21 June, 2020.

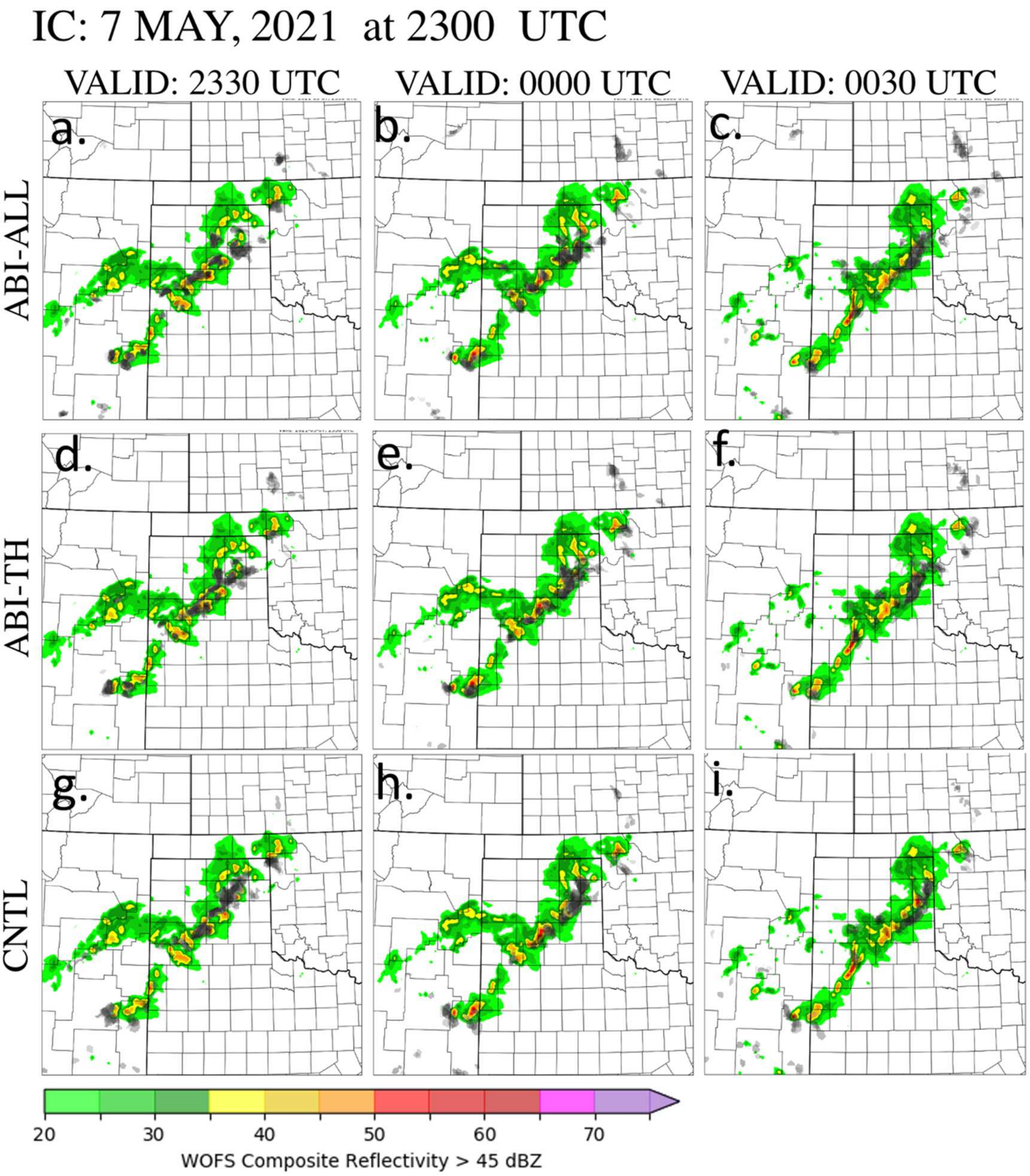

Figure 10. Same as Figure 8. but for reflectivity forecasts initialize at 2300 UTC 7 May, 2021.

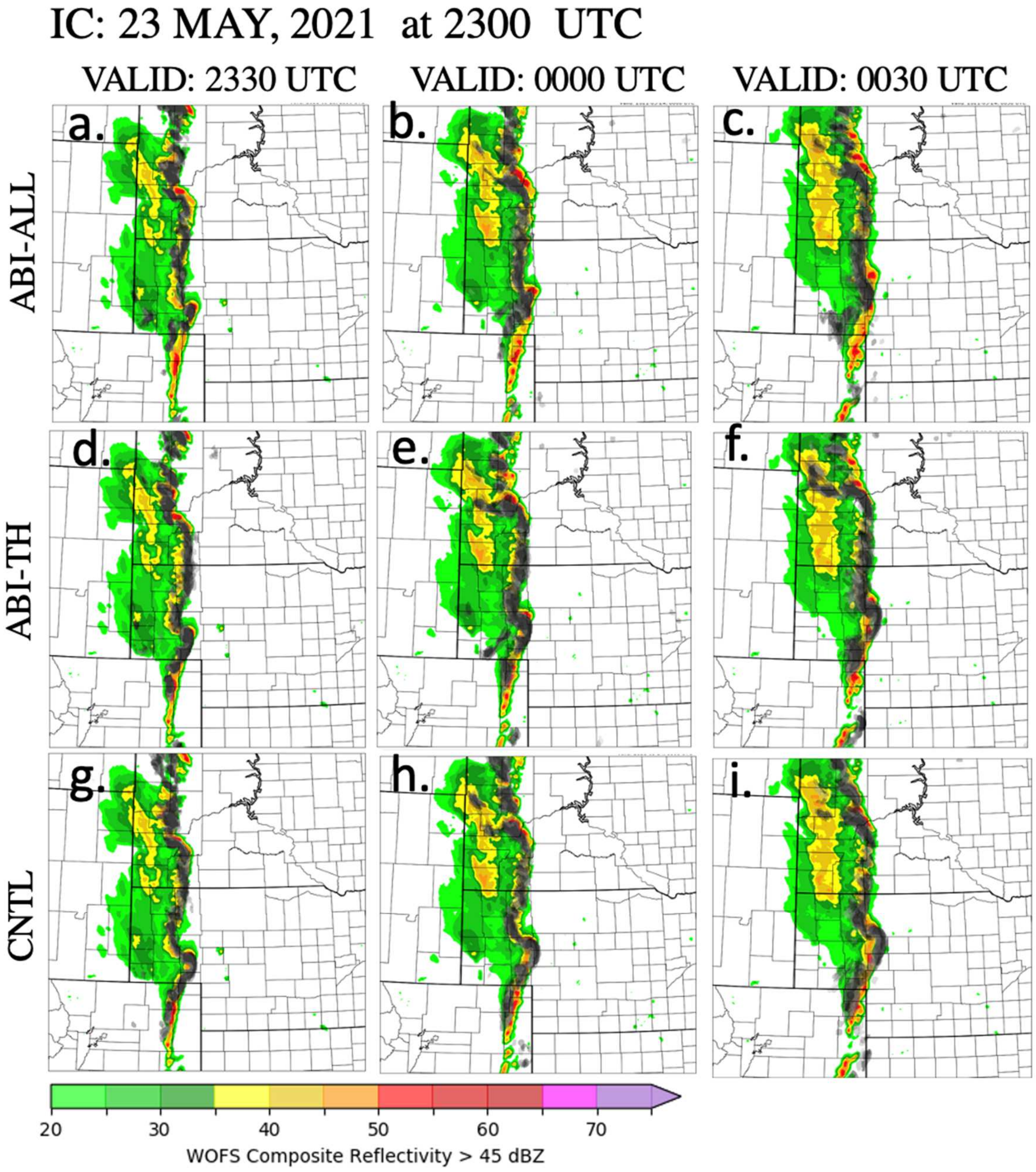

Figure 11. Same as Figure 8. but for reflectivity forecasts initialize at 2300 UTC 23 May, 2021.

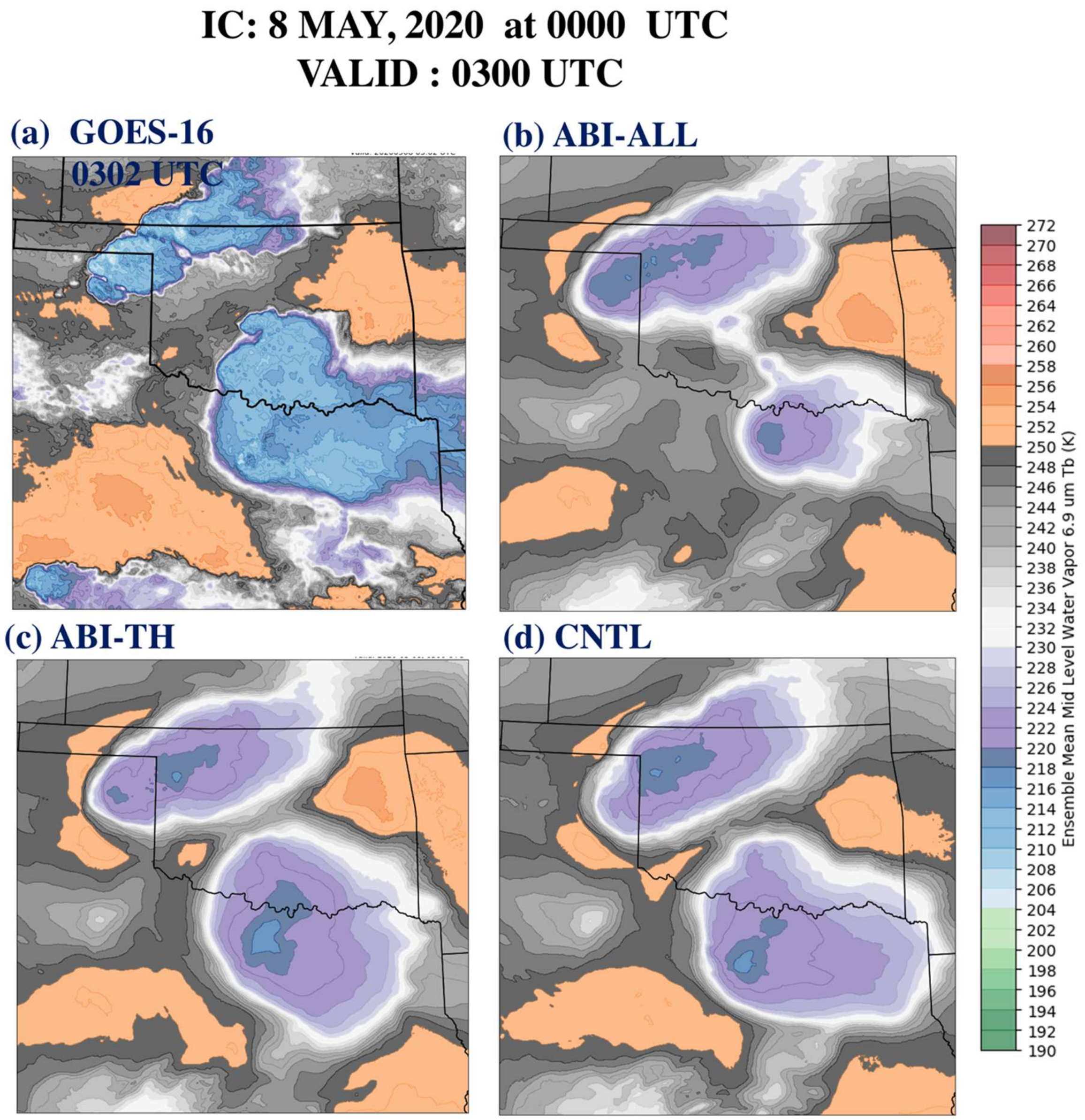

Figure 12: a comparison of (a) GOES-16 WV69 brightness temperature (K) at 0302 UTC and (b.)–(e.) ensemble mean simulated WV69 brightness temperature (K) valid at 0300 UTC for 3-h forecasts initiated at 0000 UTC 8 May, 2020.

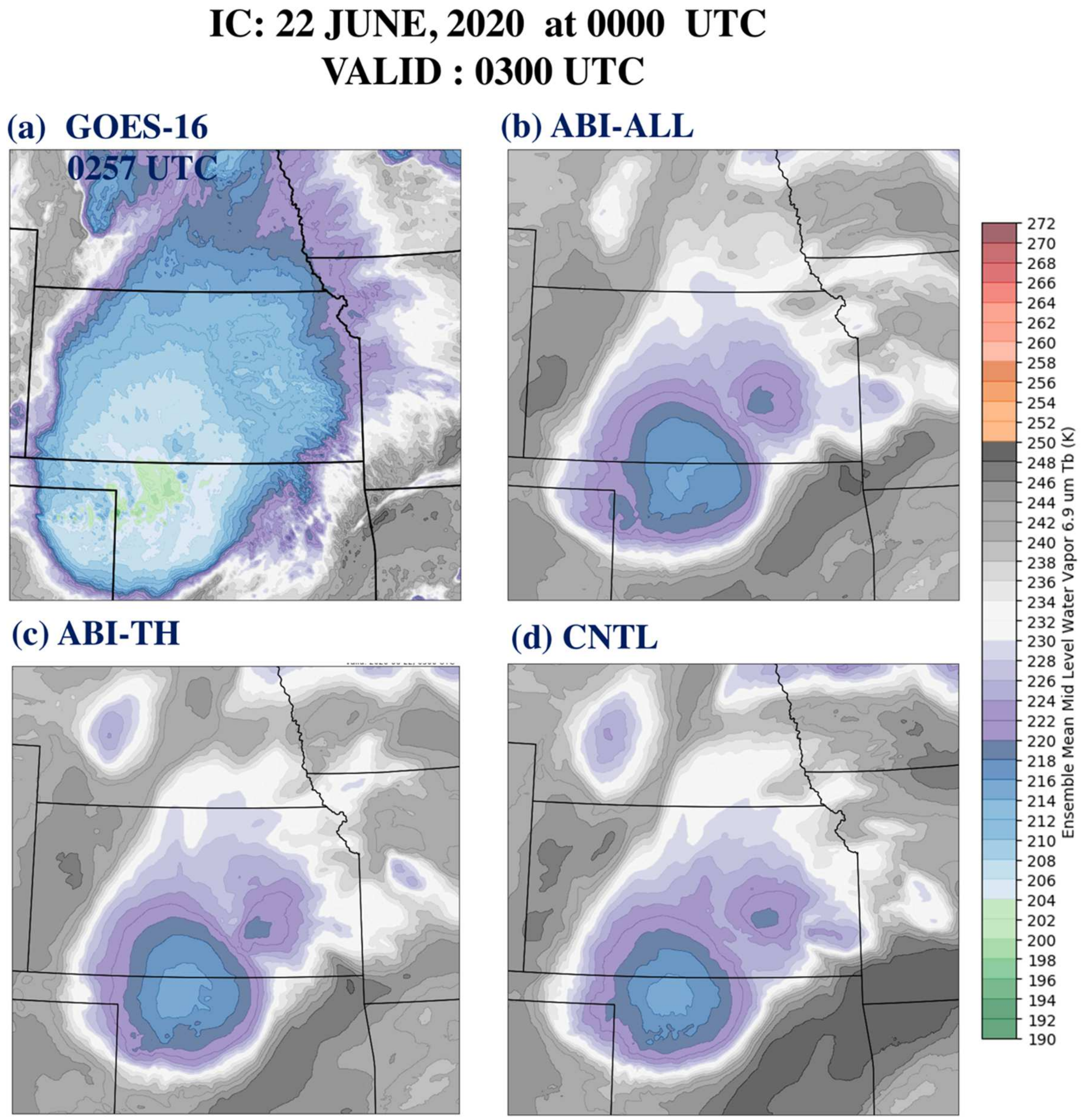

Figure 13. Same as Figure 12. but for ensemble mean WV69 brightness temperature (K) forecasts initialize at 0000 UTC 22 June, 2020.

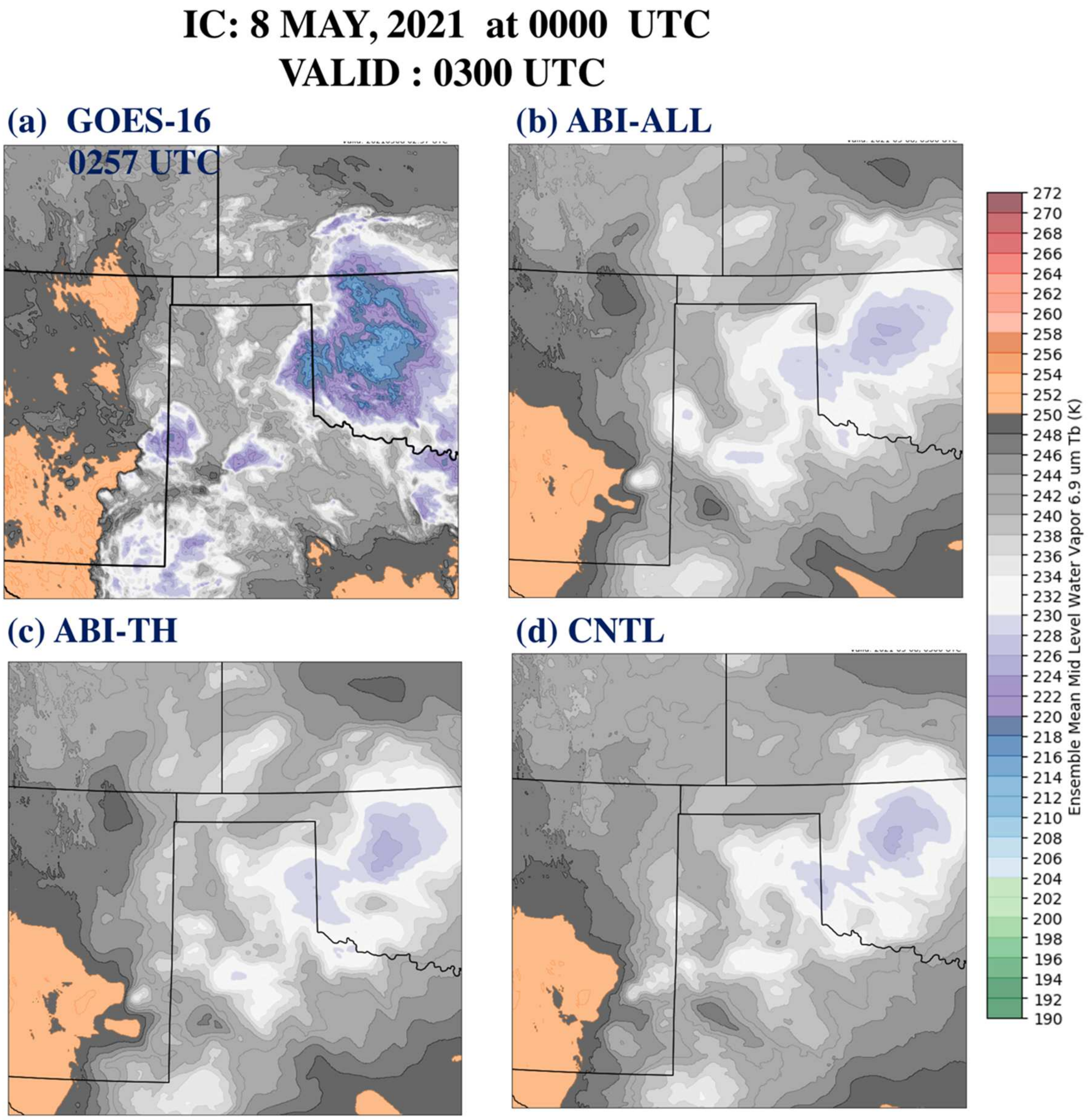

Figure 14. Same as Figure 12. but for ensemble mean WV69 brightness temperature (K) forecasts initialize at 0000 UTC 8 May, 2021.

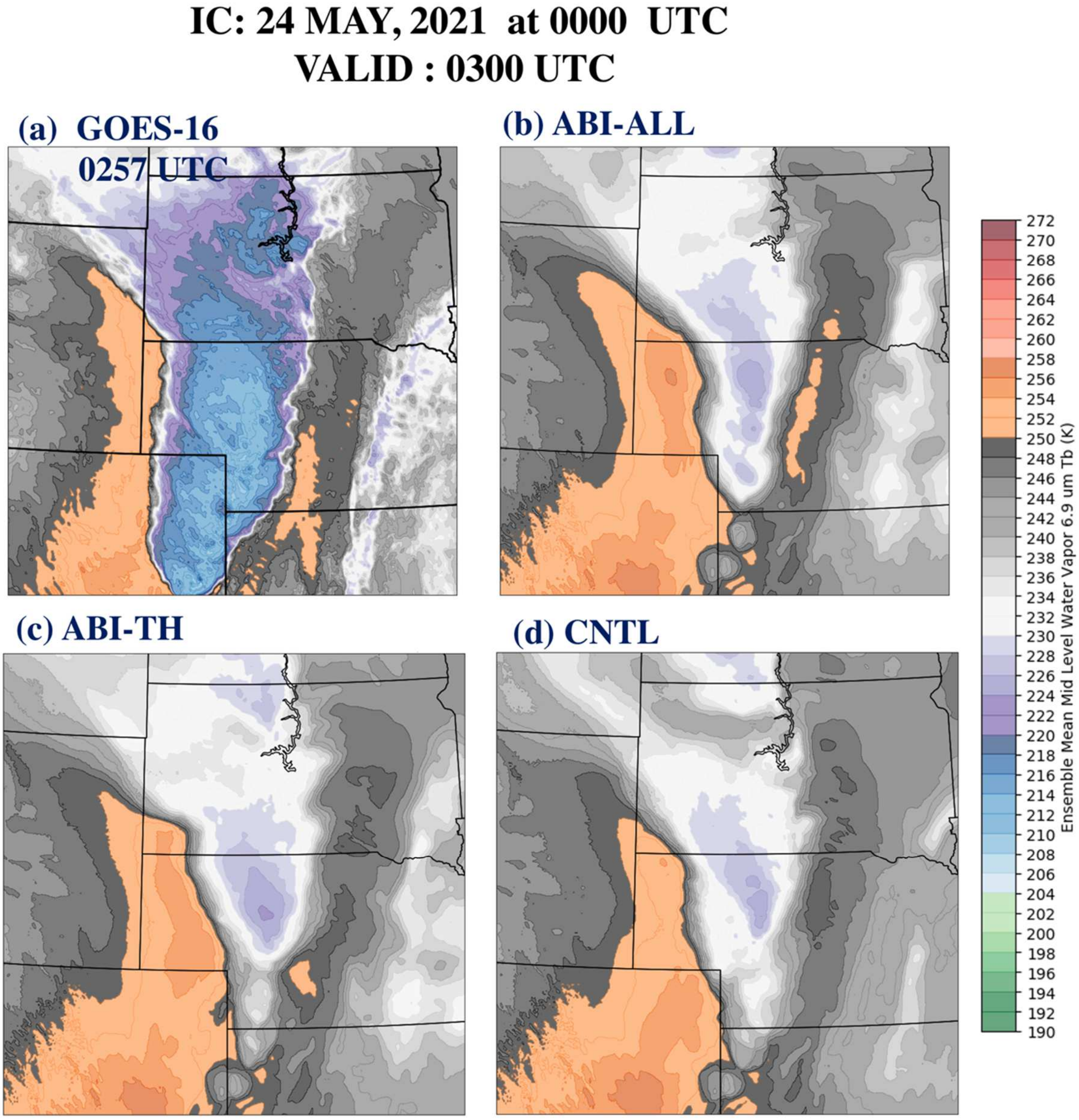

Figure 15. Same as Figure 12. but for ensemble mean WV69 brightness temperature (K) forecasts initialize at 0000 UTC 24 May, 2021.

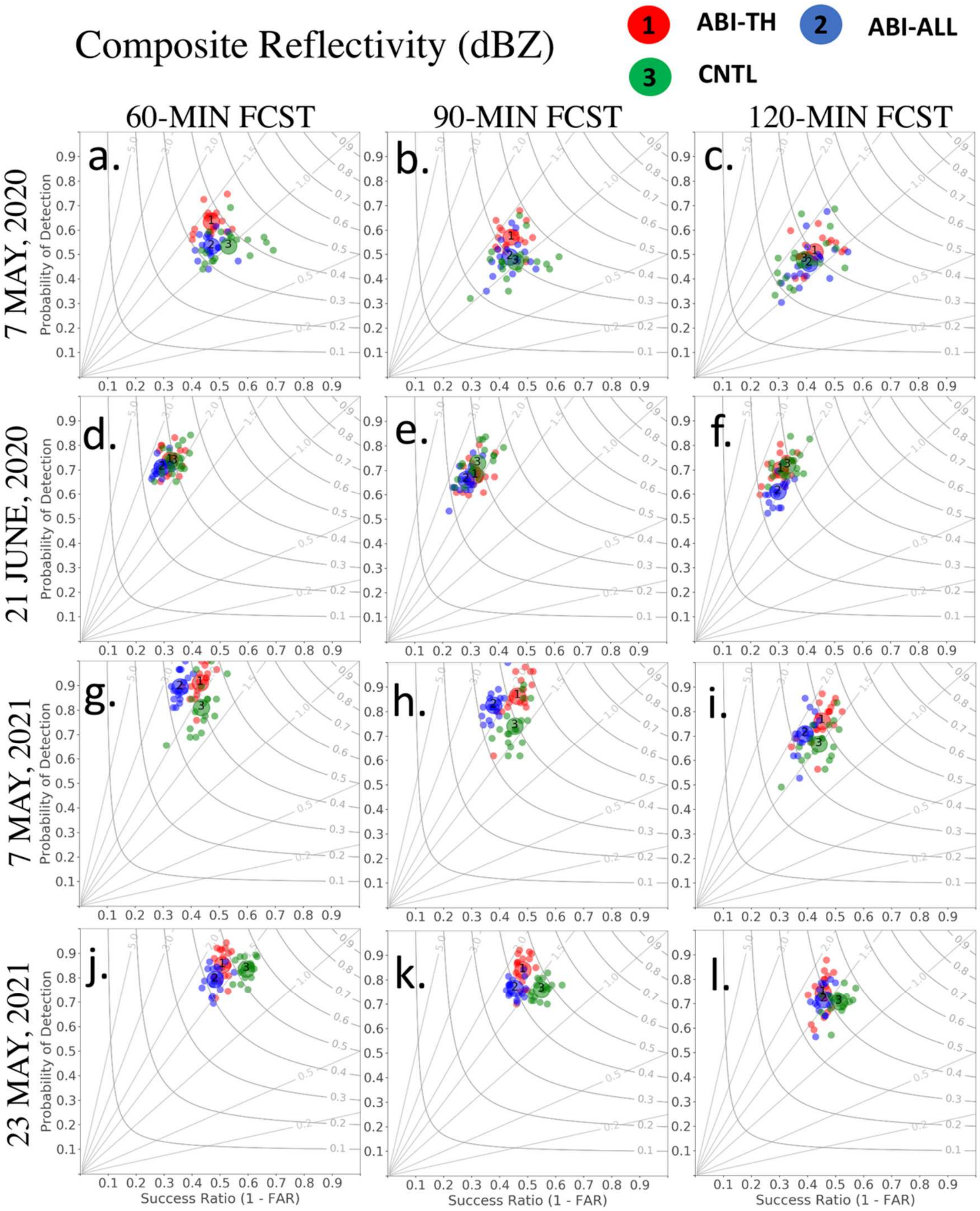

Figure 16: Performance diagram at (left) 60-min, (center) 90-min and (right) 120-min forecast time for composite reflectivity (dBZ) forecasts for 4 different events. The three different colors in all the panels represents the three types of forecasts thinned BT (ABI-TH), all BT (ABI-ALL) and all CWP (CNTL). Large dots indicate ensemble mean performances while smaller dots indicate individual member performances.

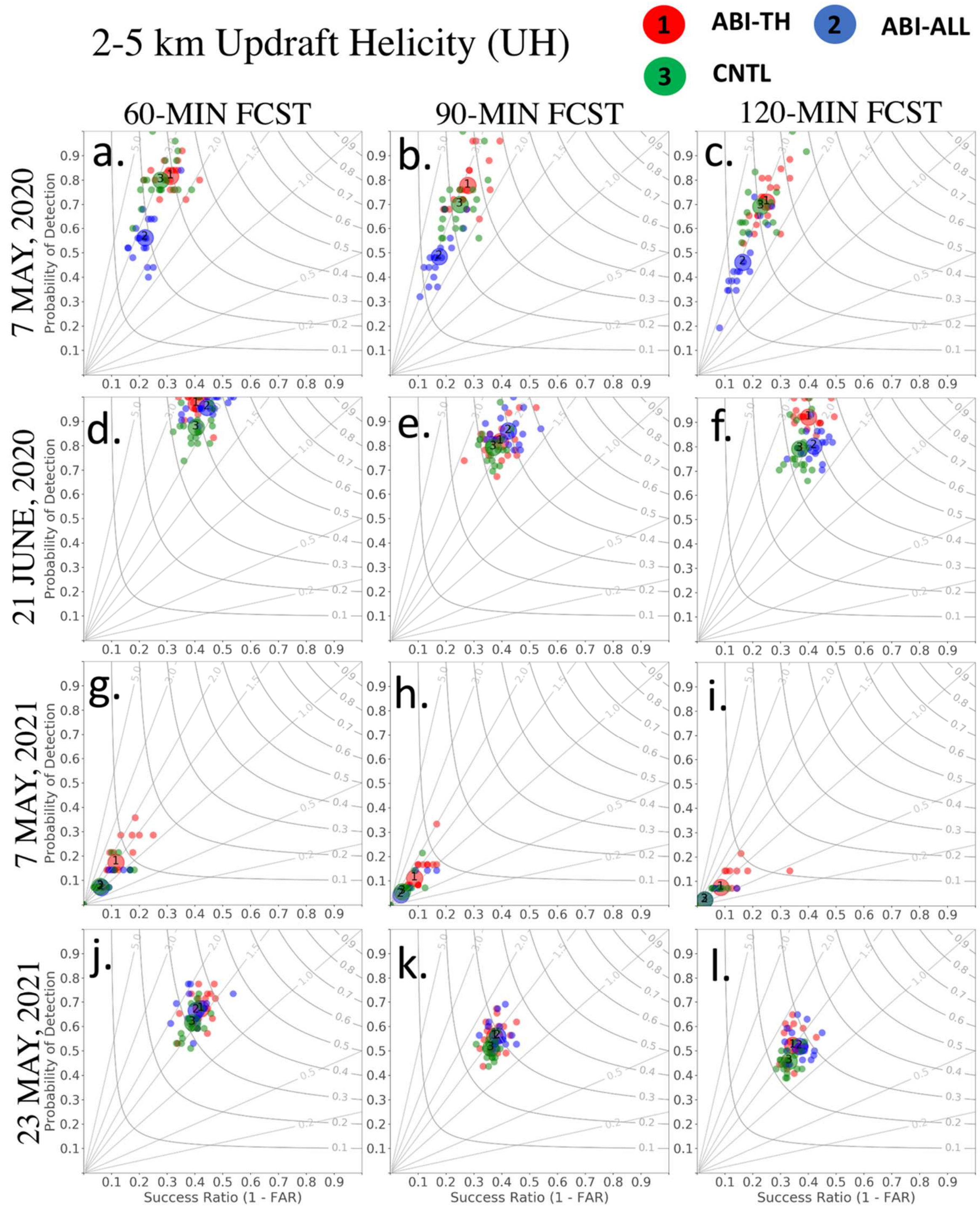

Figure 17: Same as Figure 16, but for 2-5 km Updraft Helicity (UH).